

EFFECT OF TITANIA ADDITION ON MAGNETIC
SPECTRUM AND SATURATION MAGNETIZATION
OF $\text{Ni}_{0.3}\text{Zn}_{0.7}\text{Fe}_2\text{O}_4$

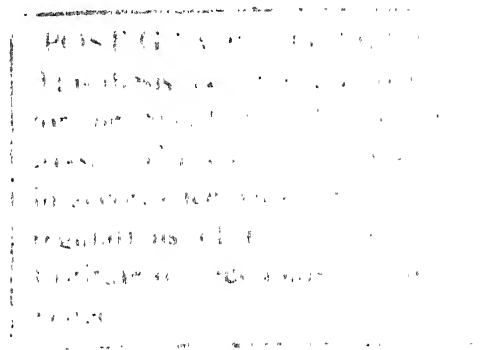
By
AMARNATH SEN



DEPARTMENT OF METALLURGICAL ENGINEERING
INDIAN INSTITUTE OF TECHNOLOGY, KANPUR
SEPTEMBER, 1978

ME
1978
M
SEN
EFF

**EFFECT OF TITANIA ADDITION ON MAGNETIC
SPECTRUM AND SATURATION MAGNETIZATION
OF $\text{Ni}_{0.3}\text{Zn}_{0.7}\text{Fe}_2\text{O}_4$**



**A Thesis Submitted
in Partial Fulfilment of the Requirements
for the Degree of
MASTER OF TECHNOLOGY**

05122

**By
AMARNATH SEN**

**to the
DEPARTMENT OF METALLURGICAL ENGINEERING
INDIAN INSTITUTE OF TECHNOLOGY, KANPUR
SEPTEMBER, 1978**

LIBRARY
55426.

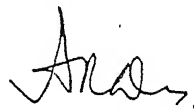
Acc. No.

13 OCT 1978 A 55426

ME-1978-M-SEN-EFF

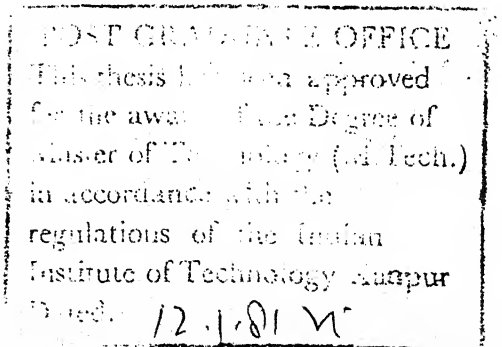
CERTIFICATE

Certified that the thesis entitled "Effect of Titanium, Zirconium and Niobium on Lattice Parameter, Density and Magnetic Saturation Moment of $\text{Ni}_{0.5}\text{Zn}_{0.5}\text{Fe}_2\text{O}_4$ " has been carried out under my supervision and it has not been submitted elsewhere for a degree.



(A. R. Das)
Professor

Department of Metallurgical Engineering
Indian Institute of Technology
KANPUR.



ACKNOWLEDGEMENTS

I owe much to Prof. A.R. Das, my thesis-supervisor, who initiated me into this project. In my journey through a problemetic path, he was my only companion with a high discursive and reflective capacity which enhanced my intellectual rigour.

I am very much indebted to Prof. E.C. Subbarao too for his generosity in allowing me to use his instruments.

I shower a lot of thanks on Mr. B. Sharma, Mr. R.K. Prasad, Mr. Malviya, Mr. K.P. Mukherjee who helped me in many ways.

I would like to mention Mr. G.C. Das, Mr. P.K. Ghosh, Mr. P.K. Nandi, Mr. N.K. Ghosh, Mr. E.M.T. Velu, Mr. S.K. Gupta, Dr. Kaul and Bulti for their kind assistance and inspiration.

Mr. R.N. Srivastava took a special interest in getting my thesis typed neatly and flawlessly. I am highly thankful to him.

- Amarnath Sen

CONTENTS

	Page
LIST OF TABLES	v
LIST OF FIGURES	vii
ABSTRACT	ix
CHAPTER I INTRODUCTION	1
CHAPTER II PRESENTATION OF PROBLEM	12
CHAPTER III EXPERIMENTAL PROCEDURE	13
A) Raw materials	13
B) Mixing	13
C) Calcination and ferritisation	13
D) Wet grinding	14
E) Particle size determination	15
F) Pressing powder preparation	15
G) Packing powder	15
H) Powder pressing	15
I) Sintering	16
J) Permeability and Q-factor measurement	17
K) Saturation magnetization measurement	19
L) Polishing and grain size measurement	19
CHAPTER IV RESULTS AND DISCUSSION	21
A) Raw materials	21
B) Calcination and ferritisation	21
C) Wet grinding	22
D) Particle size determination	22
E) Packing powder	23
F) Pressing	23
G) Sintering	24
H) Microstructure and grain size	25
I) Magnetic spectrum	26
J) Saturation magnetization	30
CHAPTER V CONCLUSIONS	37
CHAPTER VI SUGGESTIONS FOR FURTHER WORK	39
Tables	40
Figures	61
References	78
Appendix I	81
Appendix II	84

LIST OF TABLES

<u>Table</u>		<u>Page</u>
1	A.S.T.M. X-ray data for $\alpha\text{Fe}_2\text{O}_3$, NiO and ZnO	40
2	X-ray analysis of ferritised material and comparison with A.S.T.M. X-ray data for ferrite	41
3	Densification of Ni-Zn ferrites of different compositions sintered at 1250°C for 20 hrs	42
4	Densification of Ni-Zn ferrites of different compositions sintered at 1250°C for 5 hrs	43
5	Grain size of different compositions of Ni-Zn ferrite sintered at 1250°C for 20 hrs	44
6	Measurement of real and imaginary parts of initial permeability μ' and μ'' and Q-factor using parallel connection method for toroids of A batch	45
7	Measurement of real and imaginary parts of initial permeability μ' and μ'' and Q-factor using parallel connection method for toroids of B batch	46
8	Measurement of real and imaginary parts of initial permeability μ' and μ'' and Q-factor using parallel connection method for toroids of C batch	47
9	Measurement of real and imaginary parts of initial permeability μ' and μ'' and Q-factor using parallel connection method for toroids of D batch	48
10	Measurement of real and imaginary parts of initial permeability μ' and μ'' and Q-factor using parallel connection method for toroids of E batch	49
11	Measurement of real and imaginary parts of initial permeability μ' and μ'' and Q-factor using parallel connection method for toroids of F batch	50
12	Measurement of real and imaginary parts of initial permeability μ' and μ'' and Q-factor using parallel connection method for toroids of G batch	51
13	Measurement of real and imaginary parts of initial permeability μ' and μ'' and Q-factor using parallel connection method for toroids of H batch	52

<u>Table</u>	<u>Page</u>
14 Measurement of real and imaginary parts of initial permeability μ' and μ'' and Q-factor using parallel connection method for toroids of I batch	53
15 Measurement of real and imaginary parts of initial permeability μ' and μ'' for Q-factor using parallel connection method for toroids of J batch	54
16 Measurement of real and imaginary parts of initial permeability μ' and μ'' for Q-factor using parallel connection method for toroids of K batch	55
17 Measurement of real and imaginary parts of initial permeability μ' and μ'' for Q-factor using parallel connection method for toroids of L batch	56
18 Saturation magnetization of Ni-Zn ferrites of different compositions	57
19 Proposed positions of different ions in different sites in varying compositions of Ni-Zn ferrite	58
20 Chart explaining the variation of saturation magnetization in different compositions of Ni-Zn ferrites	59
21 Chart explaining the variation of saturation magnetization in different compositions of Ni-Zn ferrites	60

LIST OF FIGURES

1. Crystal structure of spinel AB_2O_4 .
2. Schematic diagram for the frequency dependence of the real and imaginary parts of the initial permeability μ' and μ'' respectively for Ni-Zn ferrite.
3. Absorption curves for a Mg-Mn ferrite (schematic).
4. Values of anisotropy constant K_1 for $Ni_{1-x}^{+2}Fe_x^{+2}Fe_2^{+3}O_4$ at 290°K with varying x.
5. Parallel connection circuit for measuring initial permeability and Q-factor of sintered toroids.
6. Calculated saturation moment at 0°K for mixed crystal series of compositions between $MeFe_2O_4$ to $ZnFe_2O_4$ where Me is Ni, Co or Mn.
7. Photomicrograph of ground ferritised particles.
8. Photomicrographs of sintered ferrites with varying percentage of Ti^{+4} (unetched).
9. Photomicrographs of sintered ferrites with varying percentage of Ti^{+4} (etched with boiling HCl).
10. Particle size distribution of ground ferritised material.
11. Frequency dependence of the real and imaginary parts of the initial permeability μ' and μ'' of different compositions of Ni-Zn ferrite sintered at 1250°C for 20 hrs.
12. Frequency dependence of the real and imaginary parts of the initial permeability μ' and μ'' of different compositions of Ni-Zn ferrite sintered at 1250°C for 5 hrs.

13. Variation of real part of initial permeability μ' with addition of TiO_2 in Ni-Zn ferrite sintered at 1250°C for 20 hrs.
14. Variation of real part of initial permeability μ' with addition of TiO_2 in Ni-Zn ferrite sintered at 1250°C for 5 hrs.
15. Saturation magnetization in Gauss cm^3/gm of Ni-Zn ferrites of different compositions.
16. M-H curve of $\text{Ni}_{0.3}\text{Zn}_{0.7}\text{Fe}_2\text{O}_4$ sintered at 1250°C for 20 hrs.

ABSTRACT

The present investigation involved the study of titania addition in $\text{Ni}_{0.3}\text{Zn}_{0.7}\text{Fe}_2\text{O}_4$ and its effect on magnetic properties like permeability, loss, saturation magnetization. Real and imaginary parts μ' and μ'' of the initial permeability μ_0 were determined on toroidal samples of Ni-Zn ferrite of compositions ranging between $\text{Ni}_{0.3}\text{Zn}_{0.7}\text{Fe}_2\text{O}_4$ to $\text{Ni}_{0.3}\text{Zn}_{0.7}\text{Fe}_{1.702}\text{Ti}_{0.298}\text{O}_4$ using type 260-AP Boonton Q-meter in the frequency range of 50 Kc/s to 10 mc/s. It had been found that for samples sintered at 1250°C for 20 hrs, μ' showed a peak at a low percentage of TiO_2 which is 0.5-1% on weight basis with respect to $\text{Ni}_{0.3}\text{Zn}_{0.7}\text{Fe}_2\text{O}_4$. For samples sintered at 1250°C for 5 hrs, the permeability gradually decreased with increasing percentage of TiO_2 except at 5%, where it showed sudden increase followed by decrease at 10% TiO_2 . Saturation magnetization (σ) result showed that at 0.5% TiO_2 , σ decreased and it again increased at 1% TiO_2 , followed by decrease at 2% TiO_2 . At 5% TiO_2 , σ increased in comparison to 2% TiO_2 sample followed by increase in σ at 10% TiO_2 . This change in σ has been explained by considering the contribution of Fe^{+2} to anisotropy constant K_1 in tetrahedral and octahedral sites. M-H curve of a sample sintered at 1250°C for 20 hrs showed H_c value of 19 oersted for $\text{Ni}_{0.3}\text{Zn}_{0.7}\text{Fe}_2\text{O}_4$ and σ value of 38.14 gauss cm^3/gm for the same.

CHAPTER I

INTRODUCTION

Magnetic oxides play an important role in the electronics industry. The whole field of high frequency telecommunication in the frequency range of 10^3 to 10^{11} Hz would look very different but for the many useful properties of ferrite. Ni-Zn ferrite is one among the group of soft ferrites. It is ferrimagnetic oxide with spinel structure. General formula of spinel is AB_2O_4 . The unit cell is closed packed cubic array of 32 oxygen ions. There are 32 octahedral interstitial sites and 64 tetrahedral interstitial sites, of these 16 of the octahedral and 8 of the tetrahedral sites are filled by cations (Fig. 1). In the normal spinel all the divalent ions are on tetrahedral A sites and the trivalent ions are on the octahedral B sites. In the inverse spinel the 8 tetrahedral sites are filled with trivalent ions and the 16 octahedral sites are equally shared between di- and trivalent ions. Magnetic ferrites are of inverse type.

Question may rise regarding the utility of Ni-Zn ferrite. Practically magnetic alloys are superior at low frequencies in comparison with ferrites with regard to permeability. At increasing frequencies eddy-current losses become increasingly important causing μ'' (imaginary part of initial permeability) to rise rapidly for the alloys. Manganese zinc ferrite then becomes more useful. Unfortunately Mn-Zn ferrite owes its relatively high

permeability to a very small crystal anisotropy¹, which in turn can only be achieved with a large concentration of ferrous ions and this renders it a poor insulator in comparison with some other ferrites. Thus the eddy current losses, although small, eventually become prohibitive at increasing frequencies. Then Ni-Zn ferrites of high resistivity are used.

Ni-Zn ferrite of composition $\text{Ni}_{0.5}\text{Zn}_{0.5}\text{Fe}_2\text{O}_4$ gives maximum M_s (saturation magnetization) and Ni-Zn ferrite of composition $\text{Ni}_{0.3}\text{Zn}_{0.7}\text{Fe}_2\text{O}_4$ gives maximum initial permeability². So from the permeability point of view, second composition is very important.

The magnetic behaviour of a ferrite is determined by its composition, exchange interaction, position of ions in different sites (A site or B site), anisotropy, microstructure etc. Composition will determine the number of magnetic ions per molecule, their Bohr magneton and resultant saturation magnetization value.

The strongest magnetic interaction is an antiparallel AB arrangement. In the absence of this interaction a much weaker antiparallel AA or BB interaction occurs. A brief review of the exchange interactions has been given by Groenour et al³.

There are site preference for different transition metal ions. In order to explain the site preference of transition metal ions in oxides, two theories have been put forward.

One has been given by Dunitz and Orgel⁴. They used crystal field theory concept which is based on purely ionic type of bonding.

Another theory has been given by Blasse⁵. He used a simplified molecular orbital approach, thus taking into account the covalent bonding between oxygen and transition metals. Both these theories predict tetrahedral site preference for d^5 , d^6 , d^7 , d^9 , d^{10} ions. Both approaches also agree that Cr^{+3} should have a strong preference for octahedral sites. No agreement is found for Ni^{+2} which shows no preference according to Blasse.

In $NiFe_2O_4$, the Fe^{+3} ions are equally divided between A and B sites, the magnetic moment of these ions are completely cancelled due to negative interaction, and the net magnetic moment of $NiFe_2O_4$ is due solely to the Ni^{+2} ions which is equal to 2 Bohr magneton.

Zn^{+2} ions have strong preference for tetrahedral sites. So in Ni-Zn ferrite, with increasing Zn^{+2} content, Fe^{+3} ions are forced into octahedral position, thereby increasing the net magnetic moment of the structure. However, the addition of Zn^{+2} ions more than 50 mole % in nickel ferrite reduces the net magnetic moment from the peak value as the AB interaction is overcome by the BB antiparallel interaction⁶.

Next important topic is anisotropy, which strongly controls the magnetic properties of the ferrites.

Anisotropy energy is by definition that part of the crystal energy that depends on the direction of magnetization. Let the direction be given by its direction cosines α_i with respect to the crystal axes. For a cubic material the energy then contains terms such as

$$E_A = K_1(\alpha_1^2 \alpha_2^2 + \alpha_2^2 \alpha_3^2 + \alpha_3^2 \alpha_1^2) + K_2 \alpha_1^2 \alpha_2^2 \alpha_3^2 + \dots \quad (1.1)$$

The anisotropy constants K_1 , K_2 etc. vary from one material to another and in addition are temperature dependent. Chemical composition can influence anisotropy. Two factors are important regarding this. First is the crystal structure and second is the type of magnetic ion.

There are two sources of anisotropy. One is due to dipolar energy. Strain induced anisotropy can be explained by this. Another source of anisotropy is from individual ions. The influence of surrounding ions on the electron orbits of the magnetic ion is taken into account by means of crystalline field. By the crystalline field the electron orbits of the ion interact with the lattice. The spins of the same electrons are coupled to the orbit by spin-orbit interaction. The orbital angular momenta of ions in the crystal lattice can differ appreciably from the values found when the ions are not built in a crystal lattice. Fe^{+2} and Co^{+2} in octahedral sites give nonzero orbital angular momenta. So due to spin-orbit coupling, anisotropy is obtained. But Fe^{+2} on tetrahedral site gives reversed sign anisotropy. In Fig. 4, with increasing Fe^{+2} content, values of K_1 have been shown for Ni-ferrite^{6A}.

Now we are in a position to discuss various types of losses and resonance⁷. The desirable properties for soft magnetic materials are high permeability and low loss. If a magnetic

field is magnetized by the a.c. magnetic field $H = H_0 e^{i\omega t}$, the magnetic flux density B is generally delayed by the phase angle δ because of the presence of loss and is thus expressed as

$$B = B_0 e^{i(\omega t - \delta)}.$$

$$\text{Permeability } \mu = \frac{B}{H} = \frac{B_0 e^{i(\omega t - \delta)}}{H_0 e^{i\omega t}} = \frac{B_0}{H_0} e^{-i\delta} = \mu' - i\mu'' \quad (1.2)$$

$$\text{where } \mu' = \frac{B_0}{H_0} \cos \delta \quad \text{and} \quad \mu'' = \frac{B_0}{H_0} \sin \delta$$

μ' expresses the component of B which is in phase with H , so it corresponds to the normal permeability. μ'' expresses the component of B which is delayed by the phase angle 90° from H . The ratio

$$\frac{\mu''}{\mu'} = \tan \delta = \text{Loss factor} = \frac{1}{Q} \quad (1.3)$$

where Q = Quality factor.

The most important loss in ferromagnetic substances is the hysteresis loss. For soft ferrites this is considerably low. The hysteresis loss becomes less important in the high frequency range, because the wall displacement, which is the main origin of hysteresis, is mostly damped in this range.

For ferrites eddy current losses are negligible because the resistivity of ferrites is high.

Magnetic after effect also gives rise to a magnetic loss for high frequency magnetization. The origin⁸ of this phenomenon

is considered to be the diffusion of electrons between Fe^{+2} and Fe^{+3} .

There is also another phenomenon, which is called dimensional resonance. If the dimension of the core is equal to an integral multiple of the wavelength λ , the electromagnetic wave will resonate within the core, giving rise to standing wave and the wavelength can be calculated by the formula

$$\lambda = \frac{c}{f \sqrt{\epsilon \mu}} \quad (1.4)$$

where c = velocity of light

f = frequency

ϵ = dielectric permittivity of the material

μ = permeability of the material.

The most important part of loss is that due to magnetic resonance. For $K_1 > 0$ (K_1 = Anisotropy constant) and the magnetization pointing along $[100]$, the resonant frequency w_r is given by

$$w_r = \gamma(H + H_a) = \gamma\left(H + \frac{2K_1}{M_s}\right) \quad (1.5)$$

where γ = Gyromagnetic ratio

H = magnetic field

H_a = anisotropic field

M_s = saturation magnetization

Resonance can also be found without applying a d.c. field. Then $w_r = \gamma H_a$. Such a situation is encountered in a measurement of initial μ . Frequency dependence of μ' and μ'' observed for Ni-Zn

ferrites of various compositions has been shown in Fig. 2.

Pil'shehikov et al⁹ have found complex absorption curves for Mg-Mn ferrite at applied field H . They explained it on the basis of domain structure and domain orientation (Fig. 3). From

$w_r = \gamma H_a$, we can get

$$f_r (\mu_{\text{rot}} - 1) = \frac{4 \gamma M_s}{3} \quad (1.6)$$

where $w_r = 2 \pi f_r$

It was first suggested by Snoek¹⁰ that the spectrum of initial permeability could be explained in terms of gyromagnetic resonance. An electron in a direct polarizing magnetic field behaves like a gyroscope. In equilibrium, the axis of the electron will be parallel to the d.c. magnetic field. If it is disturbed from its equilibrium position and then left to itself, it will tend to fall back into line with magnetic field, but it will be prevented from doing so by gyroscopic action, instead of falling back, it will precess about the magnetic field direction with a frequency dependant on the value of the magnetic field. However, if the alternating field is of the frequency set for the precession by the polarizing field, resonance occurs and the motion is large with heavy losses.

Other effects to be considered are domain wall motion and domain rotation. At lower frequencies, domain wall motion occurs, at higher frequencies domain rotation gives resonance

loss. In case of domain wall motion, loss is accompanied by relaxation. Domain patterns depend on (i) (a) M_s (b) K and (ii) microstructure. Disturbing influences are (a) growth defects (b) grain boundaries and (c) pores.

There is also another important behaviour. High initial permeability is always associated with low value of frequency at which maximum loss occurs which can be explained as below.

There is a relation that

$$\mu \approx \frac{M_s^2}{K_1} \quad (1.7)$$

Lower K_1 means higher μ . But lower K_1 also means that it is not difficult to change the direction of magnetization. The frequency of gyromagnetic resonance, which in the absence of an applied field is proportional to the anisotropy field, is therefore also low.

Considerable amount of work has been done on the effect of different additives on Ni-Zn ferrites and also other soft ferrites. Effects of cobalt on magnetite have been described by Slonczewski¹¹ and also by Bichford et al¹². Co has got a large importance because of its contribution to anisotropy. Work has also been done on the effect of cobalt addition in Ni-Zn ferrite.^{13,14,15}

A good deal of work has been done on effect of additives of different transition metal ions^{16,17} such as indium, scandium¹⁸, alkali and alkaline earths¹⁹, copper²⁰, different rare earths²¹ and also other additives²².

Very little work has been done so far on the effect of Ti and specially on Ni-Zn ferrite. Gorter²³ reported the effect of TiO_2 on Ni-ferrite and Ni-Zn ferrite. His compositions ranged from $\text{NiFe}_2\text{O}_4 - \text{Ni}_{1.5}\text{FeTi}_{0.5}\text{O}_4$ and $\text{Ni}_{1.5}\text{FeTi}_{0.5}\text{O}_4 - \text{NiZn}_{0.5}\text{FeTi}_{0.5}\text{O}_4$. They assume Ni^{+2} in octahedral sites. They were not sure regarding the positions of Ti^{+4} .

Results^{24,25} have been given on the anisotropic behaviour of $(\text{MnFe})\text{Fe}_2\text{O}_4$ and $\text{Mn}(\text{Ti}^{+4} \text{Fe}^{+2})_x \text{Fe}_{2-2x}^{+3}\text{O}_4$. In the last compound, the contribution from Fe^{+2} to K_1 and K_2 is larger by a factor of four.

Stijntjes et al²⁶ worked on the permeability and conductivity of titanium substituted Mn-Zn ferrites. He found that replacing 2Fe^{+3} by $\text{Ti}^{+4} + \text{Fe}^{+2}$ on octahedral sites in the spinel lattice yields a strongly temperature dependant positive contribution to the magnetic anisotropy. Syono²⁷ found that, in Fe_3O_4 , substitution of $\text{Ti}^{+4} + \text{Fe}^{+2}$ for 2Fe^{+3} leads to a great change in anisotropy. Measurements by Syono showed a negative contribution to K_1 which increased to lower temperatures. For larger amount of Ti^{+4} , the anisotropy become larger than 10^6 ergs/cc. This is ascribed to Fe^{+2} on tetrahedral sites.

Electrical measurements and low temperature saturation magnetization measurements done by Banerjee et al²⁸ revealed that Fe^{+2} ions occupy tetrahedral sites for most part of the solid solution series $\text{Fe}_{2-2x}^{3+} \text{Fe}_{1+x}^{2+} \text{Ti}_x^{4+} \text{O}_4$. This contributes to a large anisotropy.

Hoehne et al²⁹ also worked on induced magnetic anisotropy in titanium doped ferrites. They found that Ti doping shifted the Curie point to lower temperature.

There is another part, that is the processing part, which controls the magnetic properties to some extent. So micro-structure is very important. Domain patterns depend on micro-structure. Important magnetic properties like loss etc. depend on size, shape and orientation of domains. Complicated domain patterns have been found in polycrystalline materials, although not many observations have been made on ferrites. The grain boundary is a source of free magnetic poles because it separates two regions of different preferential directions.

Pores are usually a disadvantage for good magnetic properties. They are disturbing elements for domain movements. Linear increase of initial permeability with grain size have been found.^{30,31} Uniformity of grain size is also very important factor for good magnetic properties. A somewhat different development stems from the realization that, for high initial permeabilities at least, the extent of porosity is less important than its distribution³². More specifically, pores within the grains are very deleterious, but even large pores at the grain boundaries have surprisingly little effect.

Effect of additives may be of two types. If it remains in the grain boundary (example CaO), then it will inhibit exaggerated grain growth. If the additive enters into the

structure and is of different valency, and also if there are cation vacancies, then there will be exaggerated pore growth³³. Pores will not impede grain growth but move along with a moving grain boundary. Then they coalesce to larger pores. Then larger grain size is obtained.

The rate of grain growth can be explained by

$$(D - D_0) = Kt^{1/2} \quad (1.8)$$

where D = grain size at time t

D_0 = grain size at time, $t = 0$

K = temperature dependant constant.

Second phase inclusions and pores inhibit grain boundary migration, a limiting grain size D_e , beyond which uniform growth will not proceed, occurs at

$$D_e = \frac{d}{f} \quad (1.9)$$

where d = average size of the inclusions or pores

f = their volume fraction.

In porous ceramics the pores fill the role of growth-inhibiting inclusions and as sintering proceeds, they gradually disappear. Thus conditions for secondary recrystallization are established more or less automatically in all single phase ceramic systems at some stage in the sintering process³⁴.

CHAPTER II

PRESENTATION OF PROBLEM

Effect of Ti on ferrite is interesting from the point of view of anisotropy. We took ~~that~~ composition of Ni-Zn ferrite which is of maximum permeability i.e. $\text{Ni}_{0.3}\text{Zn}_{0.7}\text{Fe}_2\text{O}_4$. Now by adding TiO_2 , we wanted to see how the permeability changes, as permeability is related to anisotropy which is strongly affected due to addition of Ti^{+4} ions.

We also wanted to see the effect on M_s (saturation magnetization) due to addition of TiO_2 . Our composition is at the right side of the curve of Fig. 6 i.e. in the region where M_s is falling. So effect of Ti^{+4} in this region on M_s will be complex. So it is an interesting point to see how the M_s is changing with addition of Ti^{+4} and its possible explanation.

CHAPTER III

EXPERIMENTAL PROCEDURE

A) Raw Materials:

The raw materials used are noted below:

- (a) Nickel Salt - NiCO_3 , $2\text{Ni}(\text{OH})_2$, $4\text{H}_2\text{O}$ - A.R. Grade
- (b) Fe_2O_3 - A.R. Grade
- (c) ZnO - A.R. Grade
- (d) TiO_2 - L.R. Grade

All the raw materials ^{were} of fine particle size including Fe_2O_3 .

B) Mixing:

Nickel salt, Fe_2O_3 and ZnO were taken in proper amount to get the composition $\text{Ni}_{0.3}\text{Zn}_{0.7}\text{Fe}_2\text{O}_4$. Then mixing of the raw materials ~~were~~ done very carefully in small lots. The small lots were subsequently mixed again and again. As nickel salt was very fine, care was taken during mixing so that it was not lost in the air. Total 800 gm raw material was prepared. Then a small amount of moisture was added and pellets of 2" diameter were made which were used for the next stage.

C) Calcination and Ferritisation:

Then the pellets were calcined at 650°C for one and half hours. The reason for calcination was to remove gases like CO_2 ,

H_2O vapour which were formed due to decomposition of nickel salt. So the nickel oxide that was formed due to decomposition was of very fine particle size.

Then the calcined material was mixed in a porcelain pot with plastic balls for two and half hours. Note that plastic balls were used, during mixing, to avoid contamination. Then small amount of moisture was added and 2" diameter pellets were pressed. The material was ferritised at $900^{\circ}C$ for approximately 5 hrs. A small amount of ferritised powder was used for X-ray analysis on General Electric XRD-6 Model.

D) Wet Grinding:

The ferritised material was divided into 6 batches. Different amounts of TiO_2 were added to different batches. The amount of TiO_2 was batch A and G - 0%, batch B and H - 0.5%, batch C and I - 1%, batch D and J - 2%, batch E and K - 5%, and batch F and L - 10%. The percentage was calculated on weight basis with respect to $Ni_{0.3}Zn_{0.7}Fe_2O_4$ ferrite i.e. ferritised material.

Then wet grinding was done for each batch for 35 hours. The grinding was done in plastic bottles with plastic balls to avoid contamination. After grinding, slurry of each batch was put on trays and dried in oven to get powder.

E) Particle Size Determination:

A small amount of ground powder was taken. It was put in water at $\text{pH} \approx 2.5$ and stirred for 2 hours by stirrer. After proper dispersion, a drop was put on hot slide. Particles were observed under optical microscope and photographs were taken. Then curve of particle size distribution was drawn.

F) Pressing Powder Preparation:

About 1-2% polyvinyl alcohol solution was made. Then it was added to the powder of each batch and mixed uniformly. The mass was dried slowly in air to get proper moisture content.

G) Packing Powder:

It was made in the same way as pressing powder. Here the quality of the material used was of L.R. grade and directly ferritisation was done at 900°C for 6 hours.

H) Powder Pressing:

10,000 p.s.i. pressure was used and accordingly the load required was calculated. Three items were made. (a) Pellets, (b) small toroids and (c) large toroids.

Pellets were made by pressing in a split die. The diameter of the pellets was 1.29 cm. Toroids were pressed in a double pressing die. The die consisted of two parts, upper die and

the bottom die. First the pressure was applied from the top, keeping the bottom die fixed. Then the dies were turned upside down and pressure was applied to the bottom die keeping upper one fixed.

Toroids were rectangular in cross section. Small toroid was of O.D. 1.93 cm and I.D. 1.29 cm and large toroid was of O.D. 4.15 cm and I.D. 2.69 cm. Green bulk densities of the pellets and the toroids were calculated by noting the weights and by measuring the dimensions by micrometer.

I) Sintering:

Sintering was done in a 23" long horizontal tube SiC furnace. Pt, pt-10% Rh thermocouple was used as the sensing element with a controller to control the temperature to the accuracy of $\pm 1^\circ\text{C}$. The temperature was checked and corrected with an external thermocouple using d.c. potentiometer. Inside the furnace, a 2" long zone of constant temperature was obtained. First test pellets were sintered at different temperatures (1350°C , 1300°C , 1250°C and 1200°C). Sintering temperature of 1250°C was taken, as it gave maximum sintered density. 5 hrs and 20 hrs sintering time for each batch was chosen.

Toroids and pellets were sintered together in a cylindrical closed sagger, which was shaped by cutting fireclay brick. Two large toroids, two small toroids and two pellets were placed in this container and packed with packing powder. Isothermal sintering was

done for each batch. At first the furnace was heated to the desired temperature and then the container with the toroids were pushed slowly to avoid thermal shock. Then it was kept in the sintering zone for proper time and then taken out slowly. After sintering, bulk densities of the samples were taken. Porosity of the sintered material was calculated from the equation,

$$\text{Total porosity} = \frac{T_d - B_d}{T_d} \times 100\% \quad (2.1)$$

where T_d = theoretical density of ferrite

B_d = bulk density of the sintered ferrite.

J) Permeability and Q-factor Measurement:

The measurement of complex initial permeability and Q-factor was done on type 260-AP, Boonton Radio Co. Q-meter in the frequency range of 50 Kc/s to 10 Mc/s. The instrument is basically a resonant circuit from which the values of Q and inductance of the unknown coil can be directly read on a meter and a dial, respectively. The real part μ' of the initial permeability μ_o was calculated as follows³⁵:

$$\text{Inductance } L = 2 \times 10^{-7} \mu_o b N^2 \ln\left(\frac{D_2}{D_1}\right) \text{ Henry} \quad (2.2)$$

where b = height of the toroid (meter)

N = number of turns

D_2 = O.D. (meter)

D_1 = I.D. (meter)

and $\mu_o = \mu' - i \mu''$ (Equation (1.2))

$$\text{So, } L = 2 \times 10^{-7} \mu' b N^2 \ln\left(\frac{D_2}{D_1}\right) \text{ Henry} \quad (2.3)$$

$$\text{or } L_1 = \text{Constant} \times \mu' \times N_1^2 \quad (\text{For a particular toroid at } N_1 \text{ number of turns})$$

$$\text{and } L_2 = \text{Constant} \times \mu' \times N_2^2 \quad (\text{At } N_2 \text{ number of turns for same toroid})$$

$$\therefore (L_1 - L_2) = \text{Constant} \times \mu' \times (N_1^2 - N_2^2) \quad (2.4)$$

From this equation μ' was calculated. This method was used to avoid some errors which will be discussed in Appendix II.

The toroid was wound with 36 gauge insulated copper wire. Parallel connection method was used. In this case, the circuit was first resonated, using a type 590-A (Boonton Radio Co.). Standard coil of known inductance, to establish reference values Q_1 and C_1 . The circuit was re-resonated with the unknown coil connected to CAP terminals (Fig. 5) and standard coil in its original position. The altered values Q_2 and C_2 were noted and the actual values of Q and L of the unknown coil were calculated as follows:

$$Q = \frac{Q_1 Q_2 (C_2 - C_1)}{(Q_1 - Q_2) C_1} \quad (2.5)$$

$$L_p = \frac{1}{4 \pi^2 f^2 (C_2 - C_1)} \quad (2.6)$$

where L_p = inductance of the unknown coil in Henry.

K) Saturation Magnetization Measurement:

Small chips of sintered ferrites were taken from each of the six batches (A to F). Their weights were measured. Then saturation magnetization for each sample was measured in vibrating specimen Foner magnetometer. In this instrument, the specimen is forced to vibrate in a vertical direction. The a.c. signal induced by the dipole field of the specimen in a pair of secondary coils placed on both sides of the specimen is amplified and compared with a signal produced by a standard magnet, giving rise to an output signal which is exactly proportional to the magnetic moment of the specimen.

Also the magnetization and demagnetization data for a sample sintered at 1250°C for 20 hrs were taken.

L) Polishing and Grain Size Measurement:

Sintered pellets were mounted in moulds made from lucite crystals (a type of plastic). Sample mounting was done at 120°C approximately. Six samples (A to F) were mounted. Then these pellets were polished on glass plate using SiC of 100, 250, 300, 400 and 600 mesh. There were two important points in this regard. Firstly, with increase of mesh number of powder i.e. increase of fineness of powder, the grinding time was increased. Secondly, all the samples were washed carefully when the SiC powder was changed i.e. when different mesh number SiC powder was used.

Then the samples were polished in polishing wheel using $15 \mu \text{Al}_2\text{O}_3$ and finally $1 \mu \text{Al}_2\text{O}_3$. Then the samples were polished in $.3 \mu \text{Al}_2\text{O}_3$ powder. Subsequently samples were mounted in sample holders and polished in "Syntron vibratory polisher" using 1μ diamond paste and little paraffin. Here polishing was done for 30 hours. Then the photographs of unetched samples were taken in microscope. The samples were etched in 40% boiling HCl for about 10 minutes. Microphotographs of etched samples were taken. From the photographs average grain size was determined by using the formula:

$$\text{Grain size (Average)} = \frac{\sum n_i d_i}{\sum n_i} \quad (2.7)$$

where n_i = number of grains of average size ' d_i '.

CHAPTER IV

RESULTS AND DISCUSSION

A) Raw Materials:

Pure raw materials were taken (A.R. or L.R. grade). So the change in any properties due to addition of TiO_2 will be solely due to TiO_2 as there were no other impurities.

B) Calcination and Ferritisation:

The object of calcination was to remove CO_2 , H_2O from the complex Ni-salt and any other volatile impurities if present. During the decomposition of the Ni-salt, it would become finer. Finer particles, were expected to improve sintering. Ferritisation temperature of 900°C was chosen. Higher the temperature, better would be the ferritisation, but at the same time crystallites would be larger due to sintering. This would be detrimental to achieve dense sintered product. So 900°C was chosen as our ferritisation temperature. Comparison of the X-ray data of the ferritised powder and A.S.T.M. chart (Table 2) revealed that almost all the material was ferritised. There were 3 lines corresponding to 'd' values of 3.01, 1.69 and $1.2 \overset{0}{\text{\AA}}$ respectively. These lines are not present in the standard A.S.T.M. X-ray data for Ni-Zn ferrite, $\alpha\text{Fe}_2\text{O}_3$, NiO or ZnO (Tables 1 and 2). These lines may be due to formation of an intermediate phase which should disappear at 1100°C .³⁶

C) Wet Grinding:

For grinding purpose, plastic balls in a plastic bottle were used. This was to avoid any contamination. It is true that efficiency of the grinding is very poor in this condition. Since contamination could not be prevented otherwise, the lower efficiency of grinding was tolerated. Previous work of Das and Gupta³⁶ showed that assuming wear conditions with ferrite charge not more severe than empty ball load, the contamination level in the alumina jar is 0.1% per hour and in the steel balls 0.05% per hour and hence such grinding media were avoided.

D) Particle Size Determination:

In the particle size determination, main problem was of the dispersion of particles. Without proper dispersion, it was not possible to observe the size of the particles under the microscope. After trial and error, it was found that ferrite dispersed well in the pH range of 2.5. Proper stirring was done for 2 hours. Particle size distribution has been shown in Fig. 10. Maximum number of particles were in the size range of 8-10 μ . Most probably they were agglomerates, true grain size was much smaller than it. Photomicrograph of the particles has been shown in Fig. 7.

E) Packing Powder:

The reason of using packing powder was as follows. The vapour pressure of ZnO is high at sintering temperature. So some ZnO might be lost during sintering. So packing powder was used to maintain proper atmosphere, so that ZnO was not removed.

The saggar was also closed from the top with a cap. Fresh charge of packing powder was used for every sintering run.

F) Pressing:

Green densities of the sample pressed at 10,000 p.s.i. are shown in Tables 3 and 4. Maximum green density of 2.90 gm/cc was obtained. In every batch it had been found that green densities of small toroids were slightly greater than those of large toroids. This is most probably due to frictional conditions. For large toroids, the height is greater, so green composition was not uniform throughout the sample.

Das and Gupta³⁶ found that higher pressure upto 105,000 p.s.i. using much finer particle size ferrite, did not significantly increased the fired density, but led to sample cracking at the highest pressure. Hence lower pressure was used in this experiment. Second reason was the limitation of our press capacity (12,000 pound) that prevented the use of higher pressure on the large toroid. In commercial practice, however, pressure does not exceed 10,000 p.s.i. using carbide dies and punches.

G) Sintering:

Results of densification have been shown in Tables 3 and 4. Maximum sintered density of 4.42 gm/cc has been obtained in sample B sintered at 1250°C for 20 hrs. It is very low with respect to theoretical density. Higher density was not obtained because initial particle size was large. There are two factors which will control density. Firstly decrease in porosity will increase sintered density. Secondly with addition of TiO_2 , theoretical density is decreasing, hence its addition will decrease sintered density for a constant porosity material. Therefore comparison of porosity values will show in which case densification is better.

From Table 3, we note that, batch B has lower porosity than A. Then from B to F the porosity is almost constant. We know that (Ref. 33), if the additive enters into the structure and is of different valency and also if there are cation vacancies, then small pores will coalesce to larger pores and some pores will be removed. This is most probably due to increased diffusion rate. Hence the lower porosity in B is probably due to enhanced diffusion rate.

Table 4 is showing densification results for samples fired at 1250°C for 5 hrs. These results are somewhat different in comparison with materials sintered for 20 hrs. For samples sintered for 5 hrs, batch H is of low porosity in comparison to batch G. Here the trend is similar to samples sintered for

20 hrs. But for batches I, J and K, the porosity has increased gradually followed by a decrease in porosity for batch L. The sudden increase of porosity from I to K batches are not explainable at present. More thorough densification studies are required to find the cause. In conclusion, in the case of sintering for 20 hrs, the porosity first decreased then remained constant with increasing TiO_2 , while for the 5 hrs sintered material the initial decrease in porosity was followed by an increase and then a final decrease with increasing TiO_2 content.

H) Microstructure and Grain Size:

Photomicrographs of ferrites of A to E batches have been shown in Figs. 8 and 9. Grain sizes of different compositions of Ni-Zn ferrite sintered at 1250°C for 20 hrs have been tabulated in Table 5.

Average grain size of A (0% TiO_2), B (.5% TiO_2), C (1% TiO_2) batches is $4\ \mu$ and that of D (2% TiO_2), E (5% TiO_2) batches is $5\ \mu$. Grain size of batch G (10% TiO_2) is much bigger, it is $11\ \mu$. So it is clear that with increase of TiO_2 there is a tendency of increasing grain size. It can be explained after Reiguen³³. As Ti^{4+} will enter into the lattice, so there will be more coalescence of pores due to enhanced diffusion rate. In Al_2O_3 also Johnson et al³⁷ have found that TiO_2 increases grain boundary diffusion coefficient. Hence pores will not impede grain growth, but will move along with a moving grain boundary.

Then they will coalesce to larger pores. Therefore larger grains are obtained. Thus we got a tendency of increasing grain size with increasing TiO_2 , which is very prominent in 10% TiO_2 sample.

Photomicrographs of etched samples are showing that for A, B, C, D and E batches there are no intragranular pores, but there are intergranular pores. But for sample F, the grain size is much bigger and there are both intergranular and intragranular pores. During grain growth, some pores have been entrapped in this sample. In the same sample F, the grains are more or less uniform, but in other samples there is distribution of grain size. In sample F the increase in grain size is supporting our point that Ti^{+4} has entered inside crystal and TiO_2 is not present as second phase, otherwise it would inhibit grain growth and we could not get tendency of increasing grain size with increasing percentage of TiO_2 .

I) Magnetic Spectrum:

Tables 6 to 17 give the detailed information of the parameters needed to evaluate the real part μ' and imaginary part μ'' of the initial permeability and the quality factor Q of the material. From equation (1.3), we know that

$$Q = \frac{1}{\tan \delta} = \frac{\mu'}{\mu''}$$

where δ is the loss angle.

Parallel connection method was used to measure μ , Q etc. Direct coil measurement would not give material Q , but it would give only circuit Q . We could not go beyond 10 Mc/s frequency, because above 10 Mc/s the Q -response was very low and it was not possible to measure it accurately. Magnetic spectra for different samples have been shown in Figs. 11 and 12.

Let us first explain the shape of the μ' and μ'' vs. frequency curve. Figure 2 shows the schematic diagram for the frequency dependence of μ' and μ'' for Ni-Zn ferrite. This curve is somewhat ideal. We know that $w_r = \gamma(H + H_a)$, (see equation (1.5)). For initial μ , $H = 0$ and $w_r = \gamma H_a$. Since the interest of this study is in the initial part of the permeability, the loss at the resonant frequency w_r is of more significance. But when H is applied and it is sufficiently great to swamp the anisotropy fields, then the polarizing field is effectively the same everywhere in the specimen, except the shape effects. Then spread of the gyromagnetic resonance is considerably reduced and sharp peak is obtained. But Pil'shchikov et al⁹ (Fig. 3) have found complex absorption curves for Mg-Mn ferrite. They explained it on the basis of complexity of domain size, shape and orientation. So theoretically though ^{they} \angle expected one sharp peak, but they obtained complex peaks. In their case H was nonzero.

In our case $H = 0$ and $w_r = \gamma H_a$, so we can get the same effect here, because in polycrystalline samples the domain patterns are complex. So we may not get smooth curve like Fig. 2

which is ideal case and according to which Pil'shchikov should have got one sharp peak at high H value and high frequency.

In our case we got curve of more than one peak of μ'' which is not unreasonable according to above discussion. As μ' and μ'' are interrelated, so curves of μ' are not as ideal as Fig. 2.

Now the explanation of individual curves of Figs. 13 and 14 is given below. When TiO_2 is added in Ni-Zn ferrite, 2Fe^{+3} are replaced by Ti^{+4} and Fe^{+2} . Ti^{+4} ions will go to octahedral site (Ref. 26, 27). Though size of Ti^{+4} ions is comparable to that of Ni^{+2} ion, and Ti^{+4} can go to tetrahedral site, but here Ti^{+4} will go to octahedral site, as site preference depends on many factors (Ref. 4 and 5) other than size factor.

So Ti^{+4} ions will replace Fe^{+3} ions from octahedral site and equal number of Fe^{+2} will be formed from octahedral site (Ref. 26, 27, 28). The possible reason may be that the number of Fe^{+3} ions are more in octahedral sites, so Fe^{+3} ions from octahedral position will change to Fe^{+2} ions, also size of Fe^{+2} ions predicts its octahedral co-ordination (Ref. 38). With addition of more Ti^{+4} , Fe^{+2} ions will go to tetrahedral site (Ref. 26, 27, 28). The possible reason may be that as in the octahedral site, number of Fe^{+3} ions are decreasing, so Fe^{+3} ions from tetrahedral site may change to Fe^{+2} .

From anisotropy point of view, Fe^{+2} in octahedral site has positive contribution to K_1 (anisotropy constant) and Fe^{+2}

in tetrahedral site has negative contribution to K_1 (Ref. 3 and 27, Fig. 4). Effect of $\text{Fe}^{+2} + \text{Ti}^{+4}$ is much greater than only Fe^{+2} regarding contribution to K_1 .

So from the above discussion, it is clear that net anisotropy contribution associated with the addition of Ti^{+4} will be positive upto certain percentage of Ti^{+4} , then the contribution will be negative due to site change of Fe^{+2} .

In Figs. 13 and 14, the variation of μ' (real part of initial permeability) with TiO_2 is shown. It will be observed that though there is scatter in the data, the general trend is for μ' to rise to a peak at a low percentage of TiO_2 addition and then finally fall off as TiO_2 percentage is increased for samples sintered at 1250°C for 20 hrs.

This phenomenon can be explained in the following way. Initially (0.5-1% TiO_2 added sample) Fe^{+2} ions were expected to be in octahedral sites. Contribution of Fe^{+2} to K_1 in octahedral site is positive. So 0.5-1% addition of TiO_2 has decreased the net anisotropy of Ni-Zn ferrite, which is negative. We know that $\mu \approx (M_s^2/K_1)$ (equation 1.7). Change in M_s with composition is little (see Fig. 13). So due to decrease in K_1 , μ has been increased. But with more addition of Ti^{+4} , Fe^{+2} has been expected to go to tetrahedral site where it has negative contribution to K_1 . So in the latter case it will increase K_1 and hence μ will be decreased. So there is an optimum percentage of TiO_2 between 0.5-1% which will give maximum permeability and above that

optimum percentage, maximum number of Fe^{+2} ions will go to tetrahedral site. From microstructural point of view, one is expected to get higher permeability with increasing % of TiO_2 as there is a trend of increasing grain size with increase of TiO_2 percentage and it is known that permeability increases with increasing grain size (Ref. 30 and 31). But it has not been found. The reason is that the effect of anisotropy has more than overcome the effect due to grain size.

From Fig. 14 it has been observed that for samples fired at 1250°C for 5 hrs, the permeability has gradually decreased with increasing percentage of TiO_2 except at 5%, where there is a sudden increase in permeability, followed by decrease at 10%. As before for 20 hrs sintered sample, one is expected to get increase in μ in the range 0.5-1% TiO_2 . But no such has been observed.

The sudden increase of permeability at 5% TiO_2 and the absence of peak in the range of 0.5-1% TiO_2 is not explainable at present. More thorough investigation is required to find possible reasons.

J) Saturation Magnetization:

Table 18 and Fig. 13 have shown saturation magnetization of Ni-Zn ferrites of different compositions. It is to be noted that as σ is a material property and M_s depends on the porosity of the material, so the curve of σ vs. composition has been

drawn where σ is in gauss cm^3/gm and M_s is in gauss. To explain the curve we have to start from Fig. 6 which shows the saturation moment at 0°K for mixed crystal series of compositions between MeFe_2O_4 to ZnFe_2O_4 where Me is Ni, Co or Mn. Let us take NiFe_2O_4 at first. Here Fe^{+3} ions are equally distributed between A and B sites, the magnetic moments of these ions are completely cancelled due to negative interaction, and the net magnetic moment of NiFe_2O_4 is due solely to the Ni^{+2} ions, which is equal to 2 Bohr magneton. With addition of ZnFe_2O_4 , Zn^{+2} goes to tetrahedral site as it has preference for tetrahedral site. As a result, an additional Fe^{+3} ion is forced into an octahedral position, thereby increasing the net magnetic moment of the structure. But Zn^{+2} when more than 50 mole % is added, the net magnetic moment decreases from the peak value. The reason is that a number of Fe^{+3} ions will have no magnetic neighbours and hence their spins become uncoupled.

Two points are coming from this discussion. Firstly we can calculate theoretical Bohr magneton below 50 mole % ZnO , as in this range (0 to 50 mole % ZnO) straight line approximation is more valid, above 50 mole % ZnO the curve is falling.

Secondly number of magnetic ions in octahedral and tetrahedral position is important. It will control whether the spins will be coupled or not. So ratio of number of magnetic ions in octahedral position and tetrahedral position is an important parameter (the ratio has been denoted by R). It is to be noted

that although this ratio is one of the important parameters, but there are other considerations such as Bohr magneton of each ion, orientation of spins etc. which will also affect coupling. In Ni-Zn ferrite maximum M_s is found at 50 mole % ZnO i.e.

$Ni_{0.5}Zn_{0.5}Fe_2O_4$ composition. The position of ions in different sites are $Zn_{0.5}Fe_{0.5}(Fe_{1.5}Ni_{0.5})O_4$ (ions within the bracket are in octahedral position). In this case $R = 4.00$, with increasing ZnO, R will increase. So straight line approximation to calculate Bohr magneton is more valid when $R \leq 4.00$ in this case.

At $R > 4.00$, if we calculate Bohr magneton assuming straight line approximation, then we can say relatively that if the calculated Bohr magneton of one material is greater than that of another material, then actual Bohr magneton of the former is greater than that of later. Actual value of Bohr magneton will be much less than calculated value, but relatively it is possible to compare the Bohr magnetons of the materials. As for example, in Fig. 6, the B_M corresponding to point P is less than the value at Q.

Table 19 has shown proposed positions of different ions in different sites in varying composition of Ni-Zn ferrite. For 0% TiO_2 , the positions are well-known.

For 0.5% TiO_2 , we have taken all Fe^{+2} in octahedral sites. The reasons have been described during discussions of magnetic spectrum. During discussions we gave reason that Fe^{+2} ions formed during addition of TiO_2 from 0.5 to 1% will remain in

octahedral site. In batch C (1% TiO_2) total number of Fe^{+2} ions are 0.029 per molecule and in batch B (0.5% TiO_2) total number of Fe^{+2} ions are 0.015. So between 0.015 to 0.029 number of Fe^{+2} ions will be in octahedral sites. So number of Fe^{+2} ions in octahedral site is $0.015 + x$ where $0 \leq x \leq (0.029 - 0.015)$ i.e. $0 \leq x \leq 0.014$. This x is not constant according to our proposition, with increase of Ti^{+4} , most of the Fe^{+2} ions will occupy tetrahedral position, but Fe^{+2} in octahedral site will also increase in a slow rate, i.e. x will increase slowly and our upper limit of x , 0.014, may not be strictly an upper limit.

In Tables 20 and 21, R , calculated Bohr magneton (B_M), % decrease in B_M with respect to batch material A and % decrease in R with respect to batch material A have been tabulated. In Table 20, during calculation, lower limit of x (i.e. $x = 0$) has been taken and in Table 21, upper limit of x (i.e. $x = 0.014$) has been taken for calculation. In calculating B_M , we have assumed straight line approximation. Two factors will control actual saturation magnetization (σ). With decrease of R , there will be more coupling, so it will contribute in increasing σ . With decrease of B_M , σ will decrease. That is, decrease of R and decrease of B will react in opposite way.

Now we are in a position to explain σ vs. composition curve. From Tables 20 and 21, for composition B, it has been found that % decrease in R is much less than % decrease in B_M . So σ will decrease, which has been found.

For composition C, Table 20 is showing that % decrease in R is greater than % decrease in B_M . So according to Table 20, σ should increase and σ should be greater in magnitude with respect to batch material A. But experimentally increase of σ with respect to B has been found, but not with respect to A. So it is clear that % decrease in B_M is more effective in controlling σ than % decrease in R. It is highly probable that decrease in σ is proportional to (decrease in B_M)^z, where z is greater than 1. For composition C, Table 21 is showing the reverse, i.e., % decrease in R is less than % decrease in B_M . So according to Table 21, σ should decrease. It is against our experimental data, supporting our proposition that initially x is zero or close to zero.

For composition D, Tables 20 and 21 both are showing that % decrease in R is greater than % decrease in A. So apparently it may look like that here σ should increase, but it is against our experimental value. This discrepancy can be explained as follows. We have proposed that decrease in σ is proportional to decrease in B_M to the power z. We do not know the exact value of z. So, though decrease in B_M is lower in comparison to decrease in R, but decrease in σ due to decrease in B_M is greater than increase of σ due to decrease in R. So σ has decreased for composition D.

For compositions E and F both the Tables 20 and 21 are showing that % decrease in R is greater than % decrease in B_M .

For composition E, R is close to 4 and for composition F, R is less than 4. So for compositions E and F the above arguments will not hold good as they are not in the falling region of the curve (Fig. 6). Here both decrease in R and decrease in B_M have almost same weight in changing σ as here calculated and actual B_M values are almost same and B_M of a molecule is calculated by knowing the positions of magnetic ions in different sites.

So for E, as % decrease in R is greater than % decrease in B_M , so σ of E will be greater than that of D, which tally with our experimental value. For F also, % decrease in R is greater than % decrease in B_M , so here also σ will increase. We found σ of F greater in magnitude than σ of E.

There is a formula³⁹ to calculate σ ,

$$\sigma = \frac{B_M \times 5585}{\text{Molecular weight}} \text{ (Gauss cm}^3\text{/gm)}$$

We can use the calculated values of B_M for F to get values of σ . We have chosen F for this calculation; as for F, R is less than 4 (close to 2.5) so straight line approximation is more valid for F. From Table 20, we get that B_M of F = 4.45 and molecular weight of the composition F is 236.70, then we get

$$\sigma = 104.99 \text{ Gauss cm}^3\text{/gm}$$

From Table 21, B_M of F = 3.66, then we get $\sigma = 86.36 \text{ Gauss cm}^3\text{/gm}$. Our experimental value is $37.96 \text{ Gauss cm}^3\text{/gm}$.

So assumption of $x \approx 0.014$ is giving result which is more close to our experimental value. It has supported our proposition that at higher % of TiO_2 , x is 0.014 or close to 0.014. Yet there is enough discrepancy between calculated and experimental value which can be explained as follows:

- (a) σ calculated is at 0°K and σ obtained is at room temperature ($\sim 35^\circ\text{C}$) and σ at this temperature may be half of σ at 0°K (Ref. 39).
- (b) We assumed ideal structure, but there may be disorder due to processing conditions, specially rate of cooling.
- (c) Upper limit of x may not be strictly 0.014, but it is close to our proposition.

In Fig. 16, shape of the M-H curve of $\text{Ni}_{0.3}\text{Zn}_{0.7}\text{Fe}_2\text{O}_4$ sample sintered at 1250°C for 20 hrs has been shown. H_c value obtained was 19 oersted.

CHAPTER V

CONCLUSIONS

In this study of the Ni-Zn ferrite with different percentages of TiO_2 addition, the following points emerged:

1. To get contamination free grinding, grinding can be done in plastic bottle with plastic balls. But in this process grinding efficiency is very low. So very long time grinding may give fine particles.
2. Higher pressure may be used during forming and hence higher green density and finally higher sintered density may be obtained.
3. Addition of TiO_2 decreased porosity in all percentages for 20 hrs sintering at 1250°C .
4. 0.5-1% TiO_2 sample gave maximum permeability when sintered at 1250°C for 20 hrs.
5. M_s value obtained is close to values published for Ni-Zn ferrite.
6. We have proposed the existence of an optimum amount of Fe^{+2} ions, such that below it most of the Fe^{+2} will be in octahedral site and above it most of the Fe^{+2} will be in tetrahedral site and this effect showed a peak in the permeability vs. composition curve for materials sintered at 1250°C for 20 hrs. In our case the optimum % of Fe^{+2} was associated with 0.5 to 1% TiO_2 addition.

7. Hot pressing can give 100% dense material, when we can compare the effect due to TiO_2 solely, excluding effects due to pores, grain sizes and their distribution.

CHAPTER VI

SUGGESTIONS FOR FURTHER WORK

1. Grinding should be more efficient and powder should be brought below 1 μ average size. This is industrial practice to get suitable magnetic properties.
2. Higher pressure of forming is required to get good compaction and finally good sintered density.
3. Multiple samples are to be used for a given experimental point to ensure repeatability.
4. Sintering conditions of time and temperature both may be varied to obtain optimum parameters of time and temperature.
5. 0-2% TiO_2 region should be investigated more thoroughly and its effect on μ' and M_s .
6. Other cations having similar properties to Ti^{+4} may also be used for such a study.
7. Such studies can be done both below 50 mole % ZnO and above it.

Table 1

A.S.T.M. X-ray data for $\alpha\text{Fe}_2\text{O}_3$, NiO and ZnO

A.S.T.M. X-ray data for $\alpha\text{Fe}_2\text{O}_3$				A.S.T.M. X-ray data for ZnO		A.S.T.M. X-ray data for NiO	
$d(\text{\AA})$	I/I'	$d(\text{\AA})$	I/I'	$d(\text{\AA})$	I/I'	$d(\text{\AA})$	I/I'
3.66	25	0.98	10	2.81	71	2.41	91
2.69	100	0.97	2	2.60	56	2.08	100
2.51	50	0.96	18	2.47	100	1.47	57
2.28	2	0.95	6	1.91	20	1.25	16
2.20	30	0.95	12	1.62	40	1.20	13
2.07	2	0.93	6	1.47	35	1.04	8
1.83	40	0.92	6	1.40	6	0.95	7
1.69	60	0.90	25	1.37	28	0.93	21
1.63	4			1.35	14	0.85	17
1.59	16			1.30	3	0.80	7
1.48	35			1.23	5		
1.45	35			1.18	3		
1.34	4			1.09	10		
1.31	20			1.06	4		
1.25	8			1.04	10		
1.22	2			1.01	5		
1.21	4			0.98	4		
1.18	8			0.97	7		
1.16	10			0.95	1		
1.14	12			0.93	4		
1.10	14			0.90	12		
1.07	2			0.88	6		
1.05	18			0.86	1		
1.04	2			0.83	6		
1.03	2			0.82	2		
				0.82	2		
				0.81	5		

Table 2

X-ray analysis of ferritised material and comparison with A.S.T.M. X-ray data for ferrite

A.S.T.M. X-ray data for Ni-Zn ferrite		Sample ferritised at 900°C for 5 hrs	
$d(\text{\AA})$	I/I'	$d(\text{\AA})$ (Observed)	I/I' (Observed)
4.85	14	-	-
-	-	3.01	36
2.96	45	-	-
2.69	4	2.71	14
2.53	100	2.54	100
2.42	6	2.42	11
2.10	25	2.11	20
1.71	10	1.72	11
-	-	1.69	8
1.61	25	1.62	35
1.48	35	1.49	49
1.41	28	-	-
1.32	2	-	-
1.28	8	1.28	12
-	-	1.27	9
1.21	2	-	-
1.17	< 1 (broad)	-	-
1.12	4	-	-
1.09	12	1.09	11
1.04	6	-	-

Table 3

Densification of Ni-Zn ferrites of different compositions sintered at 1250°C for 20 hrs

Sample no.	Batch	% TiO ₂ with respect to Ni _{0.3} Zn _{0.7} Fe ₂ O ₄	Pressure applied (p.s.i.)	Green density gm/cc	Sintered density gm/cc	Porosity (%)	Theoretical density gm/cc
A ₁	A	0%	10,000	2.68	4.19	22	5.377
A ₂				2.63	4.17	22	
a ₁				2.73	4.37	18	
a ₂				2.74	4.37	18	
B ₁	B	0.5%	10,000	2.58	4.26	21	5.374
B ₁				2.56	4.26	21	
b ₁				2.79	4.42	18	
b ₂				2.74	4.42	18	
C ₁	C	1%	10,000	2.84	4.25	21	5.371
C ₂				2.86	4.27	21	
c ₁				2.90	4.38	18	
c ₂				2.89	4.40	18	
D ₁	D	2%	10,000	2.67	4.19	21	5.365
D ₁				2.69	4.19	21	
d ₁				2.85	4.37	18	
d ₂				2.86	4.38	18	
E ₁	E	5%	10,000	2.74	4.17	22	5.351
E ₂				2.73	4.17	21	
e ₁				2.84	4.34	19	
e ₂				2.87	4.34	19	
F ₁	F	10%	10,000	2.83	4.14	21	5.324
F ₂				2.81	4.14	22	
f ₁				2.95	4.32	18	
f ₂				2.96	4.32	18	

Note: A₁, A₂; B₁, B₂; etc. are large toroids
a₁, a₂; b₁, b₂; etc. are small toroids.

Table 4

Densification of Ni-Zn ferrites of different compositions sintered at 1250°C for 5 hrs

Sample no.	Batch	% TiO ₂ with respect to Ni _{0.3} Zn _{0.7} Fe ₂ O ₄	Pressure applied (p.s.i.)	Green density gm/cc	Sintered density gm/cc	Porosity (%)	Theoretical density gm/cc
G ₁	G	0%	10,000	2.69	4.12	23	5.377
G ₂				2.67	4.15	23	
g ₁				2.78	4.18	22	
g ₂				2.78	4.19	22	
H ₁	H	0.5%	10,000	2.66	4.20	22	5.374
H ₂				2.65	4.21	22	
h ₁				2.83	4.29	21	
h ₂				2.86	4.30	21	
I ₁	I	1%	10,000	2.71	4.11	23	5.371
I ₂				2.71	4.10	23	
i ₁				2.83	4.24	21	
i ₂				2.85	4.25	21	
J ₁	J	2%	10,000	2.67	3.81	29	5.365
J ₂				2.65	3.79	29	
j ₁				2.90	4.13	23	
j ₂				2.88	4.13	23	
K ₁	K	5%	10,000	2.79	3.77	29	5.351
K ₂				2.78	3.79	29	
k ₁				2.87	3.99	25	
k ₂				2.88	3.96	25	
L ₁	L	10%	10,000	2.76	4.11	23	5.324
L ₂				2.77	4.10	23	
l ₁				2.83	4.27	20	
l ₂				2.83	4.27	20	

Note: G₁, G₂; H₁, H₂; etc. are large toroids
 g₁, g₂; h₁, h₂; etc. are small toroids.

Table 5

Grain size of different compositions of Ni-Zn ferrite
sintered at 1250°C for 20 hrs

Sample no.	% TiO ₂ with respect to Ni _{0.3} Zn _{0.7} Fe ₂ O ₄	Composition	Average grain size (micron)
A ₁	0%	Ni _{0.3} Zn _{0.7} Fe ₂ O ₄	4
B ₁	0.5%	Ni _{0.3} Zn _{0.7} Fe _{1.985} Ti _{0.015} O ₄	4
C ₁	1%	Ni _{0.3} Zn _{0.7} Fe _{1.971} Ti _{0.029} O ₄	4
D ₁	2%	Ni _{0.3} Zn _{0.7} Fe _{1.940} Ti _{0.060} O ₄	5
E ₁	5%	Ni _{0.3} Zn _{0.7} Fe _{1.850} Ti _{0.150} O ₄	5
F ₁	10%	Ni _{0.3} Zn _{0.7} Fe _{1.720} Ti _{0.298} O ₄	11

Table 6

Measurement of real and imaginary parts of initial permeability μ' and μ'' and Q-factor using parallel connection methods for toroids of A batch

Frequency Mc/s	Sample	No. of turns	L of stan- dard coil	C ₁ $\mu\mu\text{F}$	$\bar{\epsilon}_1$	C ₂ $\mu\mu\text{F}$	Q ₂	Q	L x 10 ⁻⁵ Henry	μ'	μ''
0.05	A ₁	90 85	25 mH	407.7	63.6	3438.0 3772.5	23.1 22.6	237.25	334.68 301.41	662.42	2.79
0.1	A ₁	90 85	25 mH	102.0	113.0	856.5 950.0	17.0 16.9	144.02	336.27 298.99	742.26	5.15
0.2	a ₁	35 30	100 μH	6270.0	58.0	8542.0 9160.0	18.0 14.0	9.46	27.89 21.93	724.84	76.62
0.4	a ₁	35 30	50 μH	3127.0	64.5	3688.0 3868.0	16.0 13.0	3.81	28.24 21.38	834.30	218.98
0.8	a ₁	35 30	10 μH	3746.5	74.0	3865.0 3932.0	30.5 25.2	1.64	33.57 21.35	1486.17	906.20
1.6	a ₁	35 30	10 μH	945.0	111.5	989.0 1003.0	23.0 18.0	1.35	22.50 17.07	660.38	489.17
3.2	a ₁	30 25	5 μH	471.0	141.0	489.0 496.5	22.0 16.0	0.96	10.10 6.97	478.50	498.44
6.4	a ₁	15 12	1 μH	511.5	80.5	531.0 541.5	15.5 10.0	0.73	3.17 2.06	530.08	726.13
10.0	a ₁	15 12	1 μH	249.5	170.0	256.5 261.0	11.5 5.0	0.35	3.62 2.20	693.00	198.00

Table 7

Measurement of real and imaginary parts of initial permeability μ' and μ'' and Q-factor using parallel connection methods for toroids of B batch

Frequency Mc/s	Sample	No. of turns	L of standard coil	C ₁ $\mu\mu\text{F}$	C ₂ $\mu\mu\text{F}$	Q ₂	Q	L x 10 ⁻⁵ Henry	μ'	μ''
0.5	B ₁	90 85	25 mH	407.7	2874.0 3213.5	22.0 21.0	180.58	411.27 361.46	834.68	4.62
0.1	B ₁	90 85	25 mH	102.0	724.0 809.5	15.0 14.9	105.63	407.63 358.37	825.47	7.82
0.2	b ₁	35 30	100 μH	6270.0	8495.5 9340.0	19.0 15.5	10.02	28.48 20.64	900.11	89.83
0.4	b ₁	35 30	50 μH	3127.0	3695.0 3906.0	18.0 14.5	4.53	27.89 20.34	866.82	191.35
0.8	b ₁	35 30	10 μH	3746.5	3847.0 3904.5	31.5 26.5	1.47	39.42 25.07	1647.53	1120.77
1.6	b ₁	35 30	10 μH	945.0	981.5 994.0	25.0 20.0	1.25	27.13 20.21	794.49	638.14
3.2	b ₁	30 25	5 μH	471.0	495.0 505.0	24.0 17.0	1.47	10.31 7.28	411.26	279.77
6.4	b ₁	15 12	1 μH	511.5	522.0 525.5	15.5 10.0	0.39	5.89 4.42	677.17	1736.30
10.0	b ₁	15 12	1 μH	249.5	255.5 259.0	12.0 4.5	0.31	4.22 2.66	718.56	2317.93

Table 8

Measurement of real and imaginary parts of initial permeability μ' and μ'' and Q -factor using parallel connection methods for toroids of C batch

Frequency Mc/s	Sample	No. of turns	L of standard coil	C_1 $\mu\mu F$	Q_1	C_2 $\mu\mu F$	Q_2	Q	$L \times 10^{-5}$ Henry	μ'	μ''
0.05	C ₁	80 75	25 mH	407.7	83.6	3888.5 4405.0	22.5 21.0	262.59	291.36 253.67	705.83	2.69
0.1	C ₁	80 75	25 mH	102.0	113.0	988.0 1108.0	16.5 15.0	168.17	286.17 252.03	639.33	3.80
0.2	C ₁	35 30	100 μH	5270.0	58.0	8945.0 9957.0	18.4 16.0	11.52	23.69 17.19	790.51	68.62
0.4	C ₁	35 30	50 μH	3127.0	64.5	3795.0 4065.0	18.5 14.5	5.53	23.72 16.89	830.65	149.66
0.8	C ₁	35 30	10 μH	3746.5	74.0	3888.0 3946.0	32.0 26.5	1.92	27.99 19.85	990.03	515.64
1.6	C ₁	35 30	10 μH	945.0	111.5	982.5 1000.5	25.0 19.5	1.28	26.41 17.84	1042.26	814.26
3.2	C ₁	30 25	5 μH	471.0	141.0	485.5 492.0	22.5 15.5	0.83	17.07 13.03	758.89	914.32
6.4	C ₁	15 12	1 μH	511.5	80.5	523.5 530.0	14.5 8.5	0.41	5.15 3.34	883.35	2154.51
10.0	C ₁	15 12	1 μH	249.5	170.0	256.0 260.5	11.0 4.0	0.30	3.9 2.3	780.80	2602.86

Table 9

Measurement of real and imaginary parts of initial permeability μ' and μ'' and Q-factor using parallel connection methods for toroids of D batch

Frequency Mc/s	Sample	No. of turns	L of standard coil	C ₁ $\mu\mu\text{F}$	Q ₁	C ₂ $\mu\mu\text{F}$	Q ₂	Q	L x 10 ⁻⁵ Henry	μ'	μ''
0.05	D ₁	80 75	25 mH	407.7	83.6	4854.0 5591.0	20.8 20.3	282.74	228.09 195.66	654.85	2.32
0.1	D ₁	80 75	25 mH	102.0	113.0	1233.0 1398.0	15.0 14.5	192.08	224.18 195.66	571.03	2.97
0.2	d ₁	35 30	100 μH	6270.0	58.0	8721.0 9575.0	20.0 16.5	11.90	25.86 19.17	823.38	69.19
0.4	d ₁	35 30	50 μH	3127.0	64.5	3726.0 3955.5	19.0 15.0	5.16	26.45 19.12	902.15	174.84
0.8	d ₁	35 30	10 μH	3746.5	74.0	3864.0 3922.0	32.5 27.0	1.73	33.70 22.57	1369.84	791.82
1.6	d ₁	35 30	10 μH	945.0	111.5	991.0 1006.5	24.0 18.0	1.39	21.53 16.10	668.06	480.62
3.2	d ₁	30 25	5 μH	471.0	141.0	485.0 492.5	21.0 15.0	0.74	17.68 11.50	898.91	1214.74
6.4	d ₁	15 12	1 μH	511.5	80.5	523.5 530.0	15.5 10.5	0.45	5.13 3.34	883.95	1964.33
10.0	d ₁	15 12	1 μH	249.5	170.0	255.0 259.0	12.5 6.0	0.20	4.60 2.66	958.02	4790.10

Table 10

Measurement of real and imaginary parts of initial permeability μ' and μ'' and Q-factor using parallel connection methods for toroids of E batch

Frequency Mc/s	Sample	No. of turns	L of standard coil	C ₁ $\mu\mu\text{F}$	Q ₁	C ₂ $\mu\mu\text{F}$	Q ₂	Q	L x 10 ⁻⁵ Henry	μ'	μ''
0.05	E ₁	80 75	25 mH	407.7	83.6	4074.5 4678.5	35.0 35.0	59.59	276.58 237.47	601.50	10.09
0.1	E ₁	80 75	25 mH	102.0	113.0	1035.0 1175.5	29.0 28.5	35.73	271.75 236.18	547.69	15.32
0.2	e ₁	35 30	100 μH	6270.0	58.0	9423.0 10524.0	28.0 24.5	26.97	20.10 14.90	637.45	23.63
0.4	e ₁	35 30	50 μH	3127.0	64.5	3890.0 4147.0	26.0 22.0	10.53	20.76 15.53	641.13	60.89
0.8	e ₁	35 30	10 μH	3746.5	74.0	3885.0 3955.0	38.5 32.5	2.72	28.60 19.00	1176.83	432.66
1.6	e ₁	35 30	10 μH	945.0	111.5	1000.5 1017.5	28.5 22.0	2.23	17.84 13.66	512.41	229.78
3.2	e ₁	30 25	5 μH	471.0	141.0	485.5 493.0	24.0 17.5	0.91	17.07 11.25	843.17	925.56
6.4	e ₁	15 12	1 μH	511.5	80.5	524.0 530.0	16.5 10.5	0.51	4.95 3.34	791.19	1551.35
10.0	e ₁	15 12	1 μH	249.5	170.0	255.0 259.0	12.5 5.0	0.20	4.60 2.66	958.02	4790.10

Table 11

Measurement of real and imaginary parts of initial permeability μ' and μ'' and Q -factor using parallel connection methods for toroids of F batch

Agency	Sample	No. of turns	L of standard coil	C_1 $\mu\mu F$	Q_1	C_2 $\mu\mu F$	Q_2	Q	$L \times 10^{-5}$ Henry	μ'	μ''
OS	F ₁	80 75	25 mH	407.7	83.6	5776.0 6501.0	25.0 23.5	467.34	188.92 166.45	514.07	1.10
1	F ₁	80 75	25 mH	102.0	113.0	1468.0 1651.0	21.6 20.0	362.49	185.61 163.68	489.36	1.35
2	f ₁	35 30	100 μ H	6270.0	58.0	8132.5 8830.0	30.0 27.5	22.61	34.03 24.85	838.16	37.07
4	f ₁	35 30	50 μ H	3127.0	64.5	3598.0 3745.0	31.8 28.3	9.38	33.64 25.64	730.43	77.87
8	f ₁	35 30	10 μ H	3746.5	74.0	3833.5 3864.5	46.5 41.5	2.91	45.53 33.57	1091.99	375.25
6	f ₁	35 30	10 μ H	945.0	111.5	980.0 991.0	38.0 32.0	2.07	28.29 21.53	617.21	298.17
2	f ₁	30 25	5 μ H	471.0	141.0	479.5 482.0	35.7 26.0	0.69	29.13 22.50	715.40	1036.81
4	f ₁	15 12	1 μ H	511.5	80.5	516.7 517.0	24.5 18.0	0.19	11.90 11.25	677.73	3567.00
0	f ₁	15 12	1 μ H	249.5	170.0	251.0 251.2	21.2 15.0	0.15	16.90 14.91	729.01	4860.07

Table 12

Measurement of real and imaginary parts of initial permeability μ' and μ'' and Q-factor using parallel connection methods for toroids of G batch

Frequency Mc/s	Sample	No. of turns	L of standard coil	C ₁ $\mu\mu\text{F}$	Q ₁	C ₂ $\mu\mu\text{F}$	Q ₂	Q	L x 10 ⁻⁵ Henry	μ'	μ''
0.05	G ₁	90 85	25 mH	407.7	83.6	6250.0 6936.0	27.4 26.4	508.39	173.59 155.35	309.28	0.61
0.1	G ₁	90 85	25 mH	102.0	113.0	1568.0 1752.0	24.2 23.6	442.49	172.95 153.66	327.08	0.74
0.2	G ₁	35 30	100 μH	6270.0	58.0	10695.0 12280.0	20.5 17.2	22.35	14.32 10.54	378.85	16.95
0.4	G ₁	35 30	50 μH	3127.0	64.5	4209.5 4267.0	21.5 17.2	11.16	14.63 10.56	407.92	36.55
0.8	G ₁	35 30	10 μH	3746.5	74.0	3966.5 4026.0	32.5 26.0	38.17	18.00 14.17	383.86	100.60
1.6	G ₁	35 30	10 μH	945.0	111.5	1001.0 1021.0	23.5 17.5	1.76	17.68 13.03	466.05	264.80
3.2	G ₁	30 25	5 μH	471.0	141.0	495.5 506.5	21.5 16.0	1.32	10.10 6.97	370.72	280.85
6.4	G ₁	15 12	1 μH	511.5	80.5	540.0 552.0	14.5 10.5	0.98	2.17 1.52	261.39	266.72
10.0	G ₁	15 12	1 μH	249.5	170.0	259.0 269.0	11.5 6.0	0.63	2.02 1.10	369.96	587.24

Table 13

Measurement of real and imaginary parts of initial permeability μ' and μ'' and Q-factor using parallel connection methods for toroids of H batch

Frequency kc/s	Sample	No. of turns	L of standard coil	C ₁ $\mu\mu F$	Q ₁	C ₂ $\mu\mu F$	Q ₂	Q	L x 10 ⁻⁵ Henry	μ'	μ''
0.05	H ₁	80 75	25 mH	407.7	83.6	10550.0 12078.0	27.5 26.0	1019.02	99.99 86.89	255.34	0.23
0.1	H ₁	80 75	25 mH	102.0	113.0	2697.0 3047.0	26.5 25.5	881.42	97.70 86.09	226.29	0.26
0.2	h ₁	35 30	100 μH	6270.0	58.0	12536.0 14487.0	19.5 18.5	29.32	10.11 7.71	271.49	9.25
0.4	h ₁	35 30	50 μH	3127.0	64.5	4704.0 5109.0	20.0 17.0	9.70	10.84 7.99	231.90	23.91
0.8	h ₁	35 30	10 μH	3746.5	74.0	4057.0 4154.0	30.0 25.0	4.18	12.75 9.72	342.76	82.01
1.6	h ₁	35 30	10 μH	945.0	111.5	1014.5 1048.0	20.0 16.0	1.78	14.25 9.61	524.88	294.88
3.2	h ₁	30 25	5 μH	471.0	141.0	506.0 520.5	17.5 12.0	1.48	7.07 5.00	276.74	186.98
6.4	h ₁	15 12	1 μH	511.5	80.5	540.5 550.0	12.2 9.0	0.81	2.13 1.60	226.94	280.17
10.0	h ₁	15 12	1 μH	249.5	170.0	261.5 270.0	10.0 4.0	0.51	2.11 1.23	399.46	783.25

Table I:

Measurement of real and imaginary parts of initial permeability μ' and μ'' and Q-factor using parallel connection methods for toroids of I batch

Frequency Mc/s	Sample	No. of turns	L of standard coil	C ₁ μF	Q ₁	C ₂ μF	Q ₂	Q	L $\times 10^{-5}$ Henry	μ'	μ''
0.05	I ₁	80 75	25 mH	407.7	83.6	10825.5 12108.0	30.0 26.5	3331.61	97.35 86.68	212.13	0.06
0.1	I ₁	80 75	25 mH	102.0	113.0	2748.0 3063.5	27.5 26.0	939.85	95.82 85.63	202.59	0.22
0.2	I ₁	35 30	100 μH	6270.0	58.0	14141.0 15950.0	22.5 18.0	487.69	8.05 6.54	175.99	0.36
0.4	I ₁	35 30	50 μH	3127.0	64.5	5045.0 5510.0	22.5 17.5	21.35	8.26 6.64	188.81	8.84
0.8	I ₁	35 30	10 μH	3746.5	74.0	4132.0 4251.0	32.0 25.0	5.62	10.27 7.85	282.05	50.19
1.6	I ₁	35 30	10 μH	945.0	111.5	1060.5 1100.5	20.5 15.5	3.13	8.57 6.45	247.08	78.94
3.2	I ₁	30 25	5 μH	471.0	141.0	508.5 532.5	16.5 11.0	1.49	6.60 4.02	355.37	238.50
6.4	I ₁	15 12	1 μH	511.5	80.5	544.3 561.0	11.5 5.5	0.89	1.87 1.25	289.99	325.83
10.0	I ₁	15 12	1 μH	249.5	170.0	265.5 281.5	7.5 2.5	0.50	1.58 0.79	369.50	739.00

Table 15

Measurement of real and imaginary parts of initial permeability μ' and μ'' and Q-factor using parallel connection methods for toroids of J batch

frequency ω /s	Sample	No. of turns	L of standard coil	C_1 $\mu\mu F$	Q_1	C_2 $\mu\mu F$	Q_2	Q	$L \times 10^{-5}$ Henry	μ'	μ''
0.05	J ₁	80 75	25 mH	407.7	83.6	13592.0 15178.0	29.5 28.5	14734.70	76.93 68.66	157.62	0.01
0.1	J ₁	80 75	25 mH	102.0	113.0	3468.5 3866.5	28.5 26.5	1270.52	75.31 67.36	151.52	0.12
0.2	J ₁	35 30	100 μH	6270.0	58.0	14554.0 16433.0	22.5 16.5	48.23	7.65 6.23	161.23	3.34
0.4	J ₁	35 30	50 μH	3127.0	64.5	5205.0 5745.5	22.0 16.5	22.13	7.62 6.05	178.26	8.06
0.8	J ₁	35 30	10 μH	3746.5	74.0	4150.0 4280.0	30.0 23.5	5.50	9.81 7.42	271.36	49.34
1.6	J ₁	35 30	10 μH	945.0	111.5	1049.0 1083.5	19.0 14.0	2.52	9.52 7.13	269.09	106.78
3.2	J ₁	30 25	5 μH	471.0	141.0	494.5 500.0	15.0 10.5	0.85	10.53 8.53	227.08	267.15
6.4	J ₁	15 12	1 μH	511.5	80.5	556.5 584.0	11.0 7.0	0.98	1.37 0.85	236.90	241.73
10.0	J ₁	15 12	1 μH	249.5	170.0	275.0 290.5	8.0 3.5	0.84	0.99 0.62	168.56	200.66

Table 16

Measurement of real and imaginary parts of initial permeability μ' and μ'' and Q-factor using parallel connection methods for toroids of K batch

frequency /s	Sample	No. of turns	L of standard coil	C ₁ $\mu\mu F$	Q ₁	C ₂ $\mu\mu F$	Q ₂	Q	L x 10 ⁻⁵ Henry	μ'	μ''
0.05	K ₁	80 75	25 mH	407.7	83.6	10806.0 12504.5	34.7 33.5	1513.58	97.53 83.84	266.43	0.18
0.1	K ₁	80 75	25 mH	102.0	113.0	2771.0 3138.0	33.3 32.0	1237.47	94.99 83.51	223.42	0.18
0.2	k ₁	35 30	100 μH	6270.0	58.0	12583.5 14835.0	26.0 22.5	47.31	10.03 7.40	261.04	5.52
0.4	k ₁	35 30	50 μH	3127.0	64.5	4717.0 5218.5	24.3 20.0	58.43	9.96 7.57	237.22	4.06
0.8	k ₁	35 30	10 μH	3746.5	74.0	4065.0 4194.5	33.0 27.8	5.03	12.39 8.84	352.36	70.05
1.6	k ₁	35 30	10 μH	945.0	111.5	1031.0 1065.0	22.0 17.0	2.58	11.51 8.25	323.57	125.41
3.2	k ₁	30 25	5 μH	471.0	141.0	502.0 522.5	18.5 13.5	1.40	7.98 4.80	373.02	266.44
6.4	k ₁	15 12	1 μH	511.5	80.5	549.0 565.5	13.5 9.5	1.18	1.65 1.14	203.11	172.13
0.0	k ₁	15 12	1 μH	249.5	170.0	262.5 273.0	10.5 3.5	0.58	1.95 1.07	350.46	604.24

Table 17

Measurement of real and imaginary parts of initial permeability μ' and μ'' and Q-factor using parallel connection methods for toroids of L batch

Frequency Mc/s	Sample	No. of turns	L of standard coil	C ₁ $\mu\mu\text{F}$	Q ₁	C ₂ $\mu\mu\text{F}$	Q ₂	Q	L x 10 ⁻⁵ Henry	μ'	μ''
0.05	L ₁	80 75	25 mH	407.7	83.6	32270.0 36281.0	25.3 24.2	2835.47	31.83 28.27	80.73	0.03
0.1	L ₁	80 75	25 mH	102.0	113.0	8262.0 9232.0	28.0 27.0	2989.01	31.07 27.77	52.62	0.02
0.2	L ₁	35 30	100 μH	6270.0	58.0	16885.0 20485.0	19.0 17.0	48.03	5.97 4.45	140.03	2.92
0.4	L ₁	35 30	50 μH	3127.0	64.5	5846.0 6740.0	20.3 19.0	25.81	5.82 4.38	132.66	5.14
0.8	L ₁	35 30	10 μH	3746.5	74.0	4355.0 4574.0	31.5 27.5	8.90	6.50 4.78	158.45	17.80
1.6	L ₁	35 30	10 μH	945.0	111.5	1112.5 1170.5	24.0 20.0	5.40	5.91 4.39	140.03	25.93
3.2	L ₁	30 25	5 μH	471.0	141.0	530.0 555.0	19.2 15.0	2.78	4.19 2.94	136.09	48.95
6.4	L ₁	15 12	1 μH	511.5	80.5	572.0 612.5	16.1 10.5	2.37	1.02 0.61	151.54	63.94
10.0	L ₁	15 12	1 μH	249.5	170.0	272.0 291.0	11.0 8.5	1.01	1.12 0.61	188.51	186.64

Table 18

The saturation magnetization of Ni-Zn ferrites of different compositions

Batch	Composition	σ gauss cm ³ /gm	$4\pi M_s$ gauss
A	Ni _{0.3} Zn _{0.7} Fe ₂ O ₄	38.14	2096
B	Ni _{0.3} Zn _{0.7} Fe _{1.985} Ti _{0.015} O ₄	36.32	2020
C	Ni _{0.3} Zn _{0.7} Fe _{1.971} Ti _{0.029} O ₄	37.41	2066
D	Ni _{0.3} Zn _{0.7} Fe _{1.940} Ti _{0.060} O ₄	34.75	1909
E	Ni _{0.3} Zn _{0.7} Fe _{1.850} Ti _{0.150} O ₄	37.95	2071
F	Ni _{0.3} Zn _{0.7} Fe _{1.702} Ti _{0.298} O ₄	37.96	2061

Table 19

Proposed positions of different ions in different sites
in varying composition of Ni-Zn ferrite

Batch	Composition
A	$\text{Zn}_{0.700}^{+2}\text{Fe}_{0.300}^{+3} [\text{Ni}_{0.300}^{+2}\text{Fe}_{1.700}^{+3}] \text{O}_4$
B	$\text{Zn}_{0.700}^{+2}\text{Fe}_{0.300}^{+3} [\text{Ni}_{0.300}^{+2}\text{Fe}_{1.670}^{+3}\text{Fe}_{0.015}^{+2}\text{Ti}_{0.015}^{+4}] \text{O}_4$
C	$\text{Zn}_{0.700}^{+2}\text{Fe}_{0.300}^{+3}\text{Fe}_{0.014-x}^{+2} [\text{Ni}_{0.300}^{+2}\text{Fe}_{1.642}^{+3}\text{Fe}_{0.015+x}^{+2}\text{Ti}_{0.029}^{+4}] \text{O}_4$
D	$\text{Zn}_{0.700}^{+2}\text{Fe}_{0.300}^{+3}\text{Fe}_{0.045-x}^{+2} [\text{Ni}_{0.300}^{+2}\text{Fe}_{1.580}^{+3}\text{Fe}_{0.015+x}^{+2}\text{Ti}_{0.060}^{+4}] \text{O}_4$
E	$\text{Zn}_{0.700}^{+2}\text{Fe}_{0.300}^{+3}\text{Fe}_{0.135-x}^{+2} [\text{Ni}_{0.300}^{+2}\text{Fe}_{1.400}^{+3}\text{Fe}_{0.015+x}^{+2}\text{Ti}_{0.150}^{+4}] \text{O}_4$
F	$\text{Zn}_{0.700}^{+2}\text{Fe}_{0.300}^{+3}\text{Fe}_{0.283-x}^{+2} [\text{Ni}_{0.300}^{+2}\text{Fe}_{1.104}^{+3}\text{Fe}_{0.015+x}^{+2}\text{Ti}_{0.298}^{+4}] \text{O}_4$

Note: 1) Ions at the left side of the bracket are in tetrahedral position. Ions within the bracket are in octahedral position.

2) $0 \leq x \leq 0.014$, details regarding x have been discussed in text.

Table 20

Chart explaining the variation of saturation magnetization in different compositions of Ni-Zn ferrite

(Assuming $x^* = 0$)

Batch	$\frac{N_1}{N_2} = R^{**}$	Bohr magneton*** per molecule in B_M	% decrease in R with respect to batch material A	% decrease in B_M with respect to batch material A
A	6.66	7.60	-	-
B	6.62	7.51	0.60	1.18
C	6.23	7.31	6.46	3.82
D	5.49	6.88	17.57	9.47
E	3.94	5.62	40.84	26.05
F	2.43	4.45	63.51	41.45

* For x see Table 19 and text.

** N_1 = No. of magnetic ions in octahedral sites

N_2 = No. of magnetic ions in tetrahedral sites.

*** B_M has been calculated assuming straight line approximation which is not true for all values of R, but it will give an idea regarding the actual Bohr magneton relatively.

Table 21

Chart explaining the variation of saturation magnetization in different compositions of Ni-Zn ferrite

(Assuming $x^* = 0.014$)

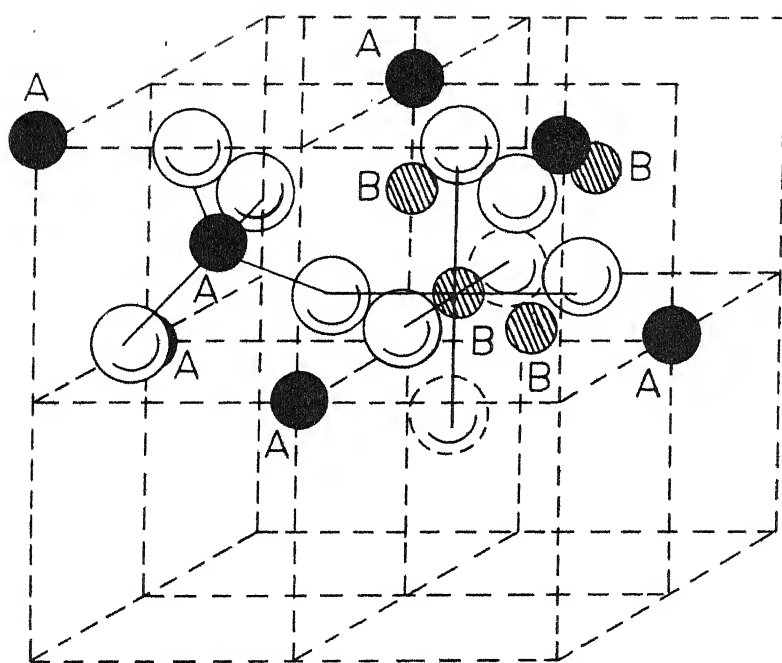
Batch	$\frac{N_1}{N_2} = R^{**}$	Bohr magneton*** per molecule in B_M	% decrease in R with respect to batch material A	% decrease in B_M with respect to batch material A
A	6.66	7.60	-	--
B	6.62	7.51	0.60	1.18
C	6.57	7.43	1.35	2.24
D	5.77	6.99	13.50	8.03
E	4.11	5.73	38.28	24.61
F	2.52	3.66	62.16	51.84

* For x see Table 19 and text.

** N_1 = No. of magnetic ions in octahedral sites

N_2 = No. of magnetic ions in tetrahedral sites.

*** B_M has been calculated assuming straight line approximation which is not true for all values of R, but it will give an idea regarding the actual Bohr magneton relatively.



A - Tetrahedral position

B - Octahedral position

Fig.1-The crystal structure of spinel AB_2O_4

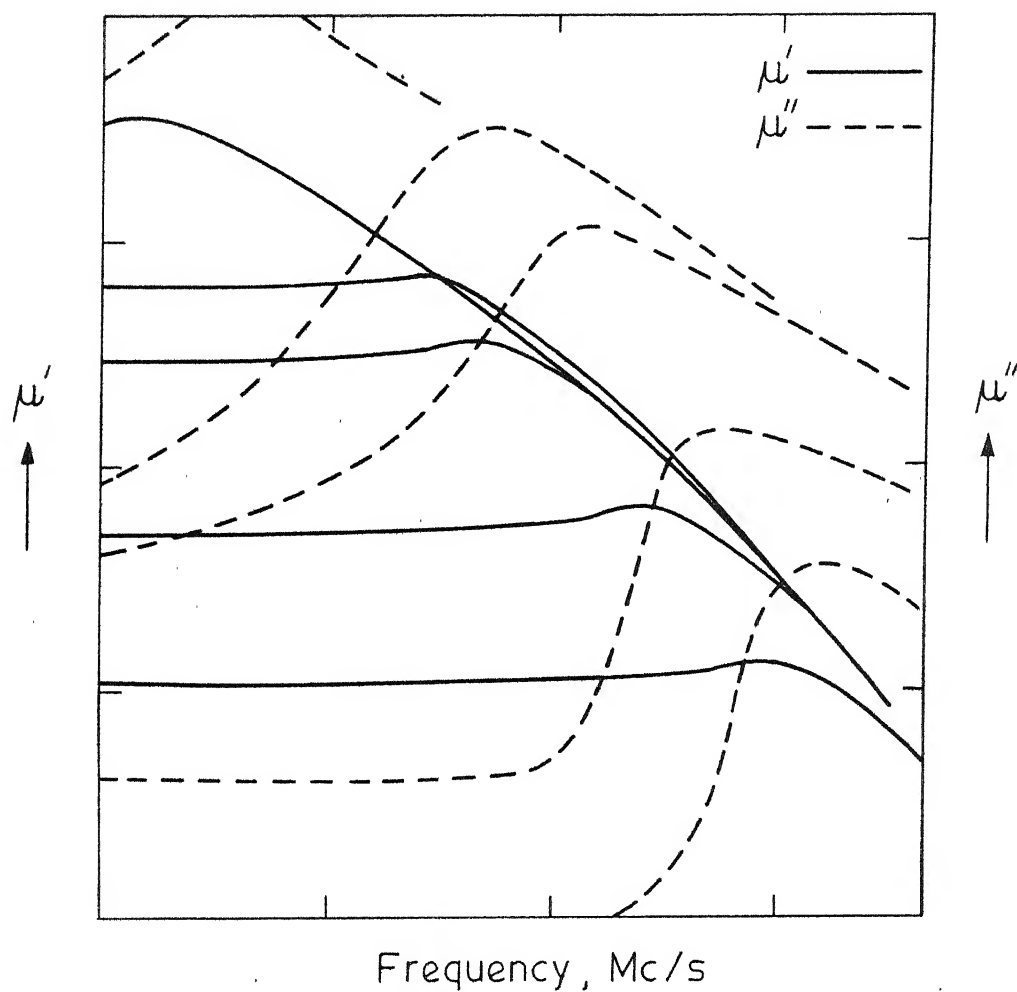


Fig. 2-Schematic diagram for the frequency dependence of the real and imaginary parts of the initial permeability μ' and μ'' respectively, for Ni - Zn ferrite.

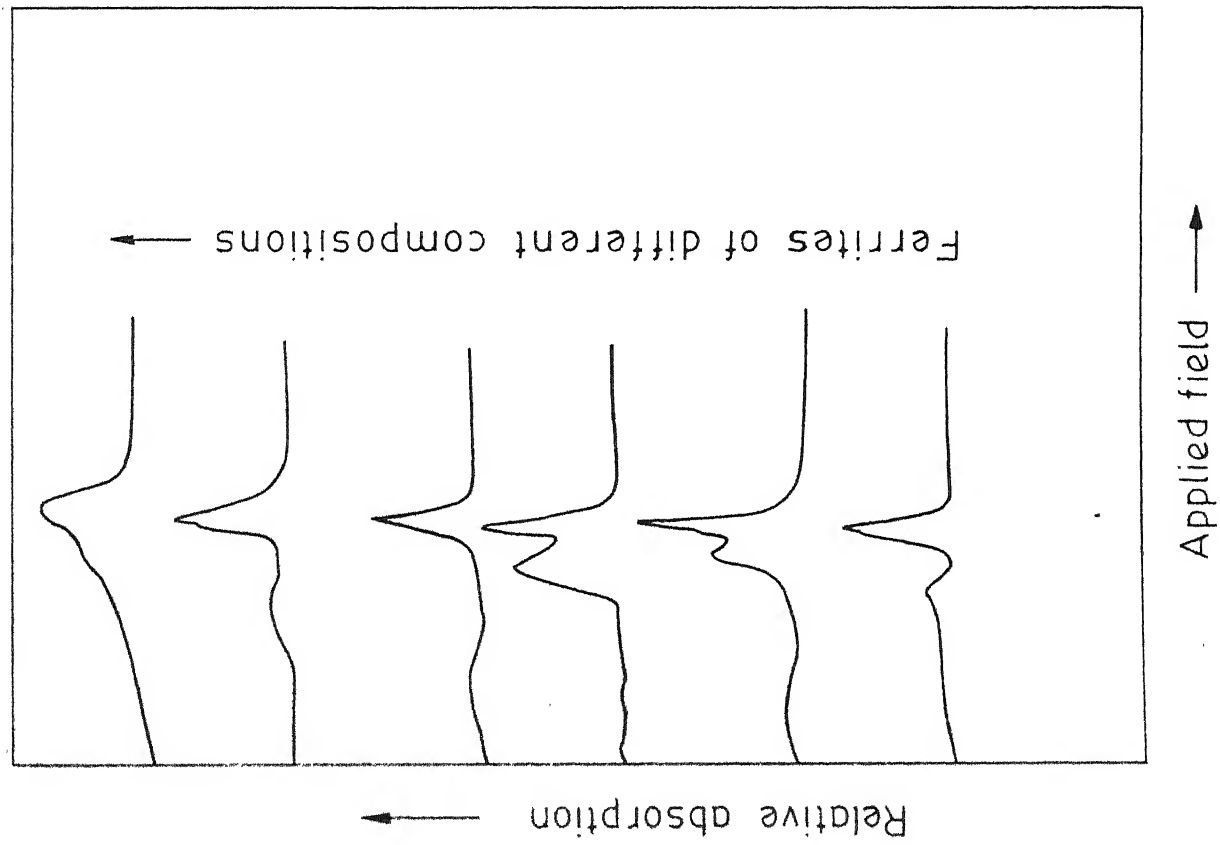


Fig.3-Absorption curves for a (schematic)
Mg - Mn ferrite. (Ref. 9)

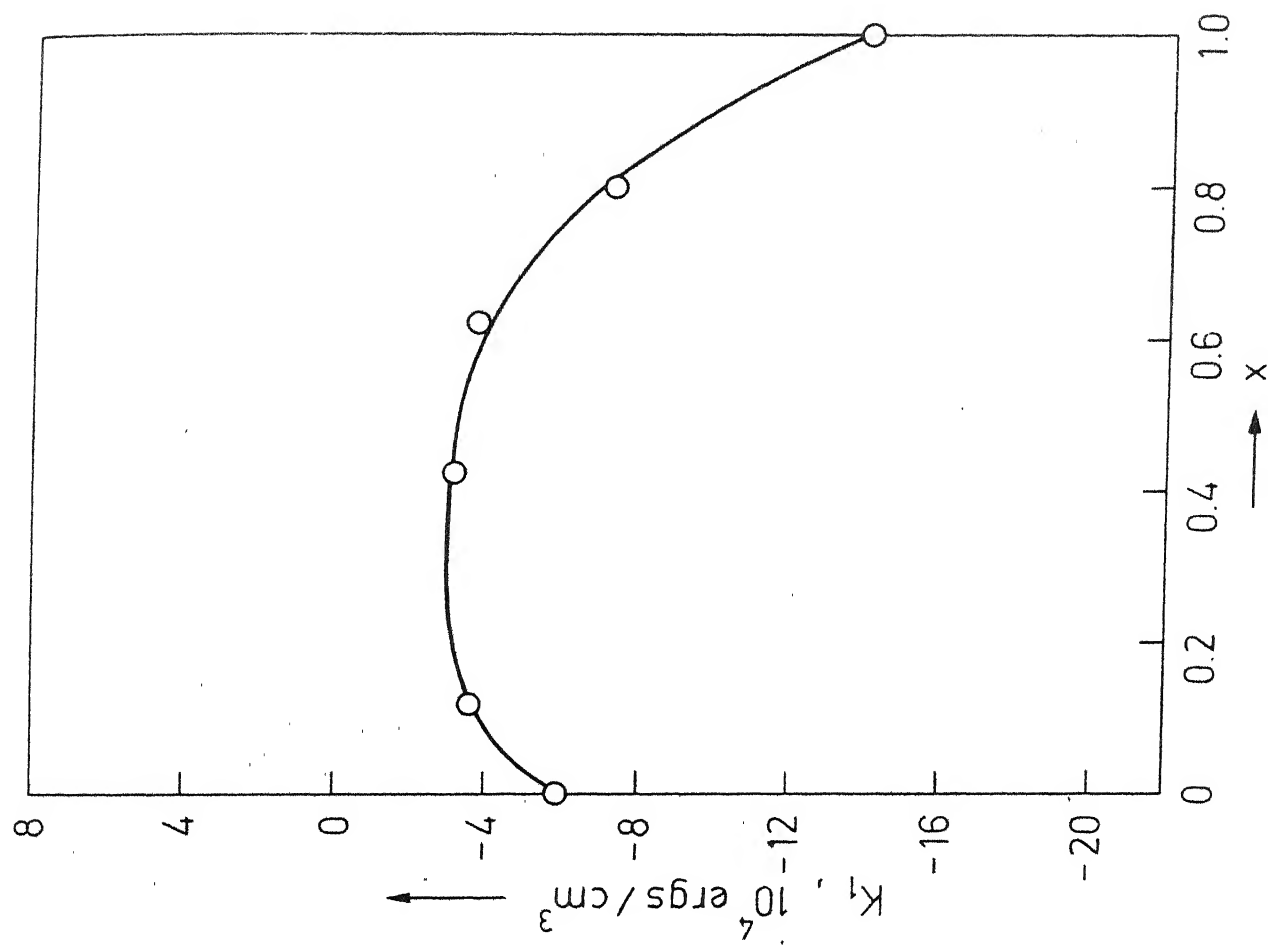


Fig.4- Values of anisotropy constant K_1 for
 $\text{Ni}_{1-x}\text{Fe}_x^{+2}\text{Fe}_2^{+3}\text{O}_4$ at 290°K with varying x .
(Ref. 6A)

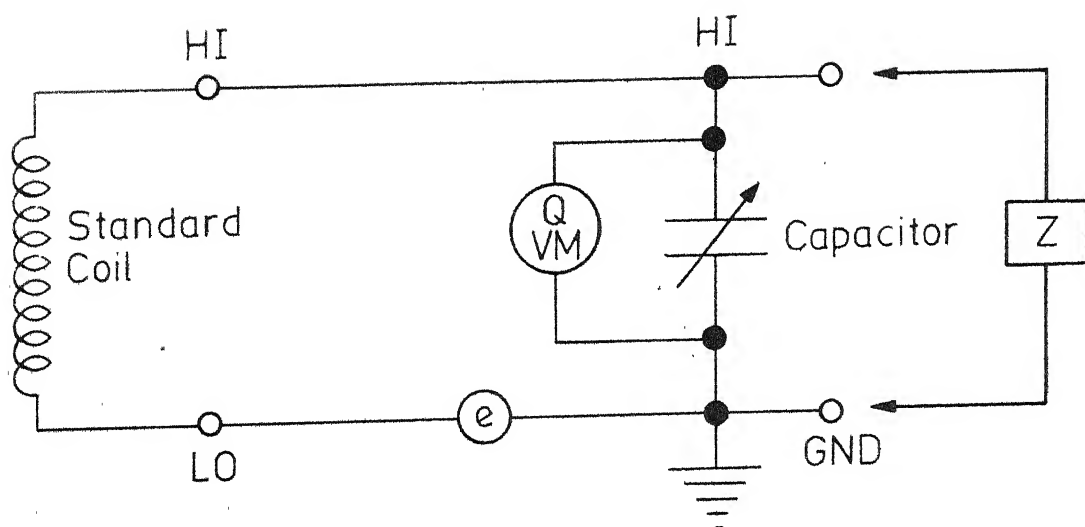


Fig. 5 - Circuit for measuring initial permeability and Q - factor of the sintered toroids.

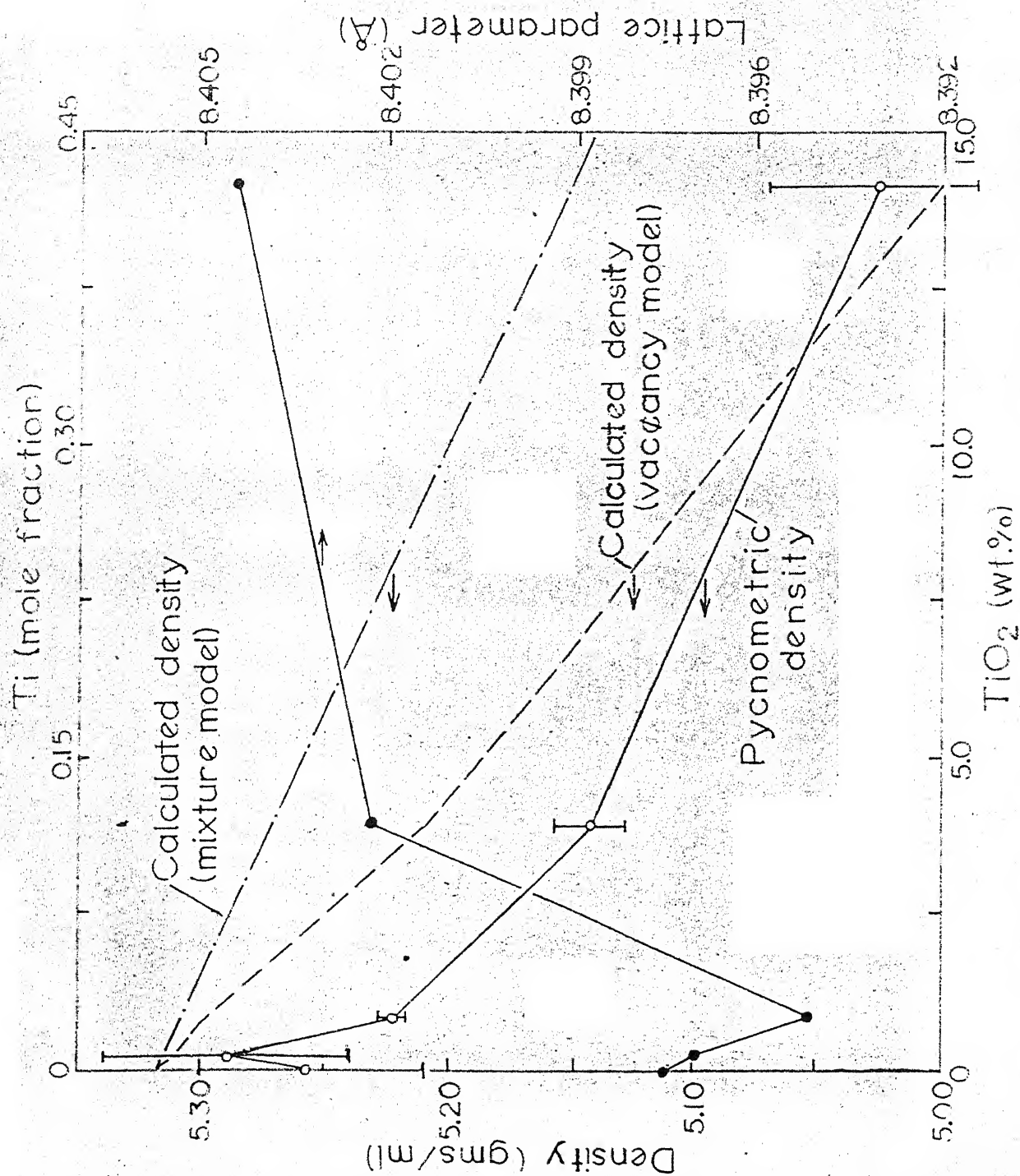


Fig. 6 Plots of density and lattice parameter for Ti-doped Ni-Zn-ferrite

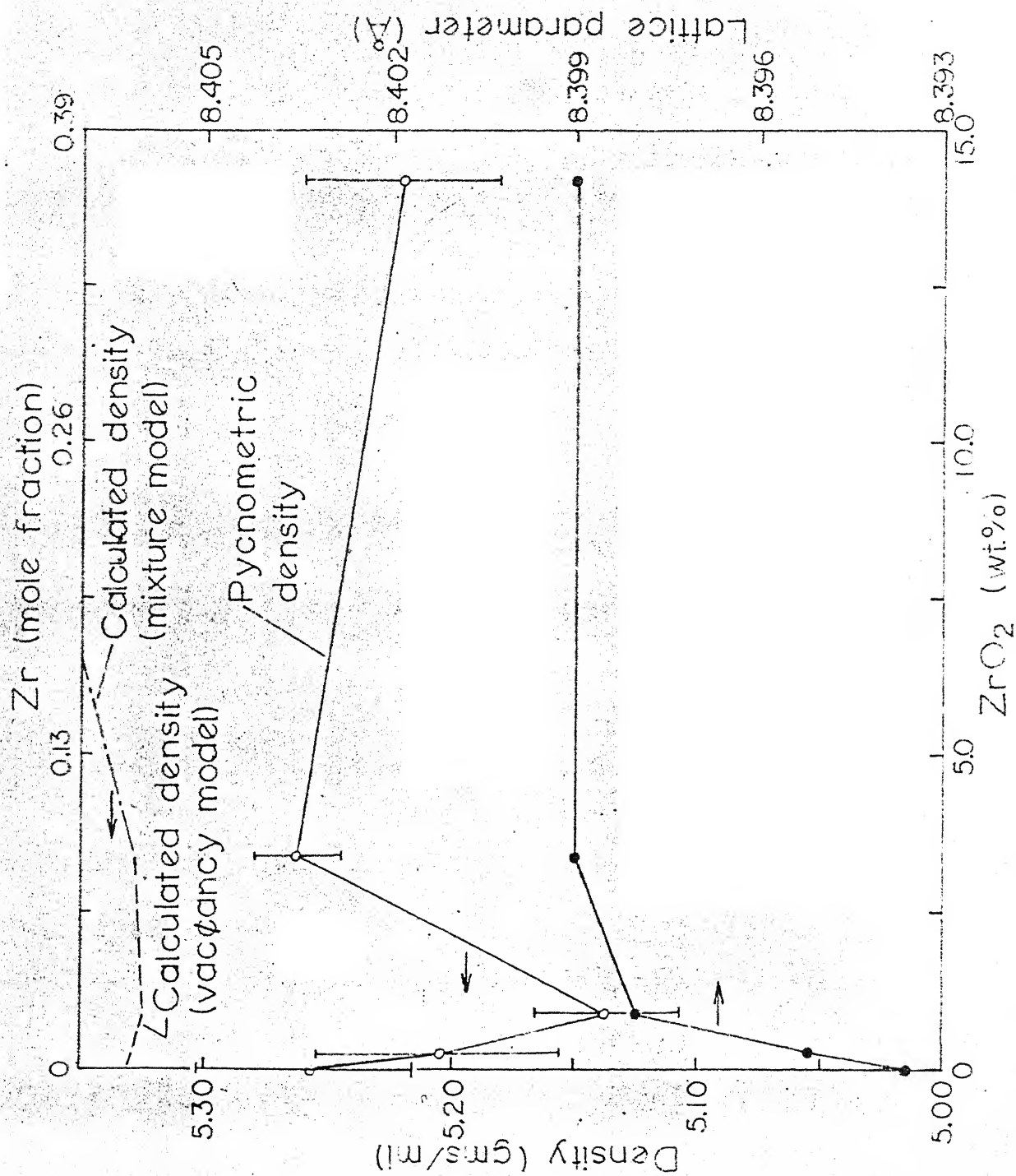


Fig. 7 Plots of density and lattice parameter for Zr-doped Ni-Zn-ferrite

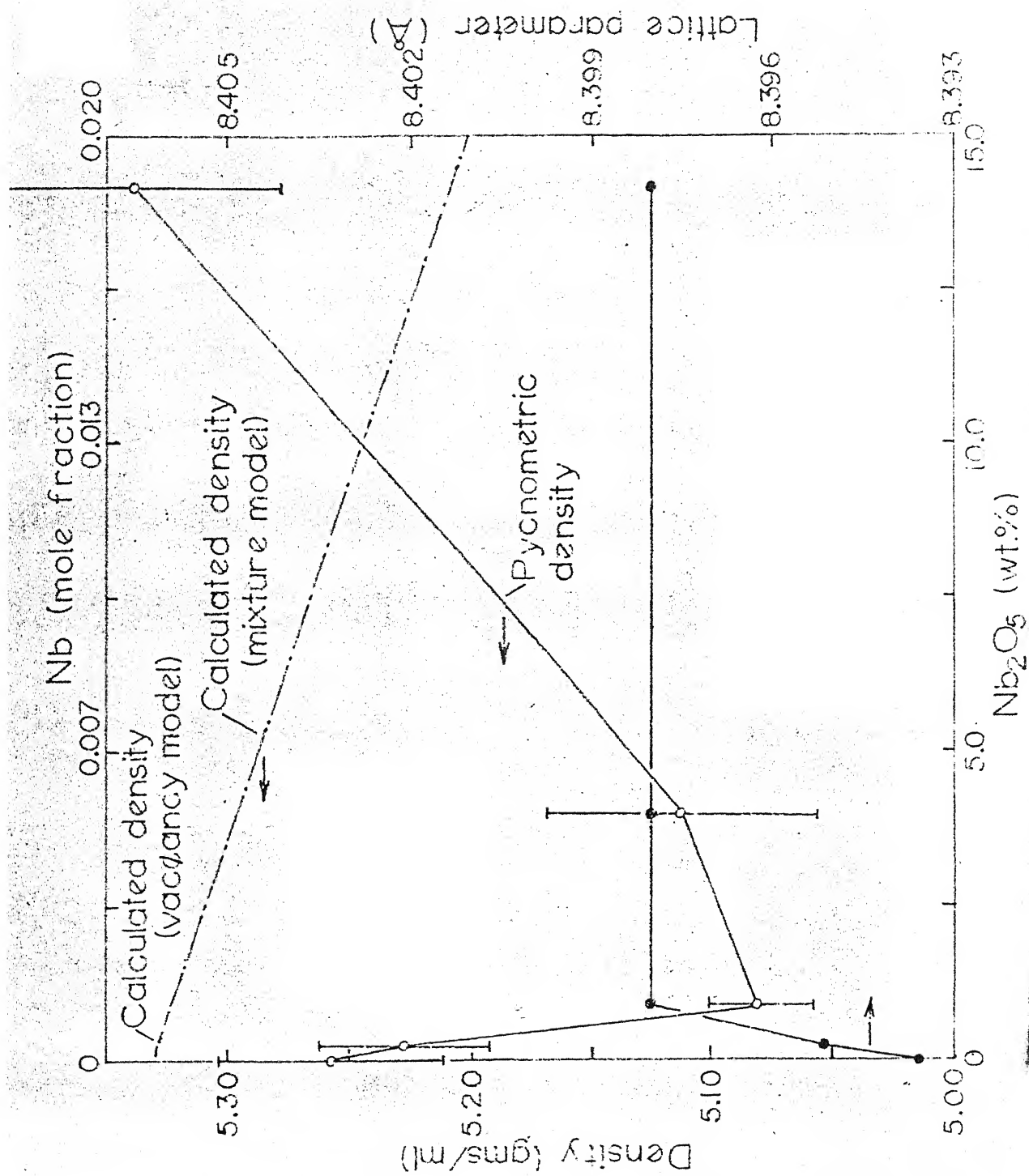


Fig. 3 Plots of density and lattice parameter for Nb-doped Ni- δ n-ferrite

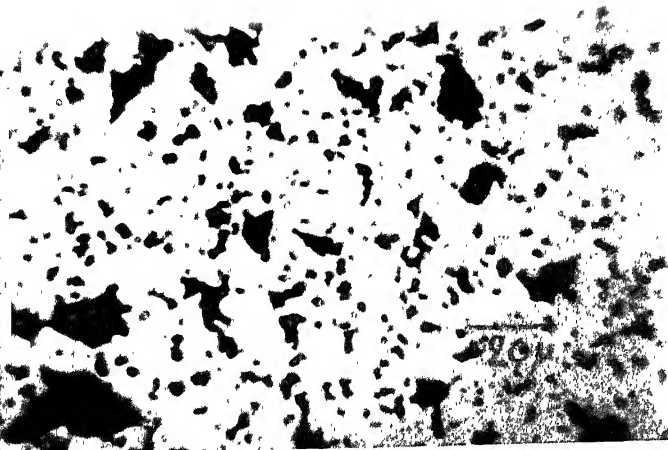


Fig. 8(iv)

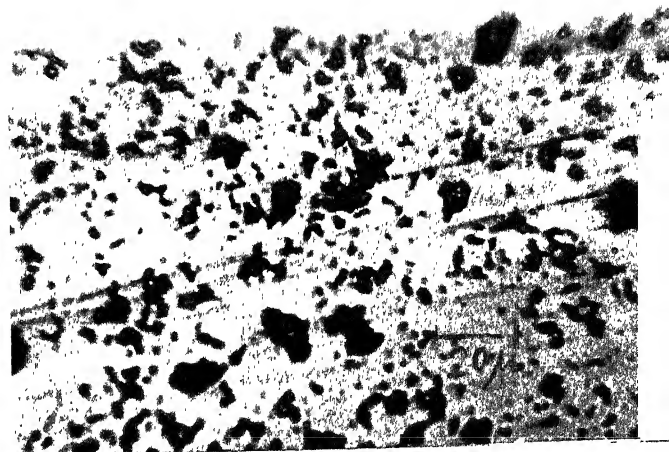


Fig. 8(v)

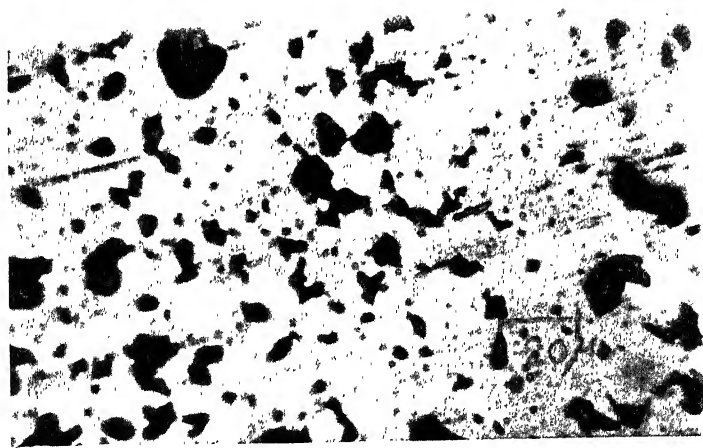


Fig. 8(vi)

Fig. 8. Photomicrographs of sintered ferrites with varying percentage of Ti^{+4} (unetched)

8(iv) Sintered at 1250°C for 20 hrs, 2% TiO_2

8(v) Sintered at 1250°C for 20 hrs, 5% TiO_2

8(vi) Sintered at 1250°C for 20 hrs, 10% TiO_2

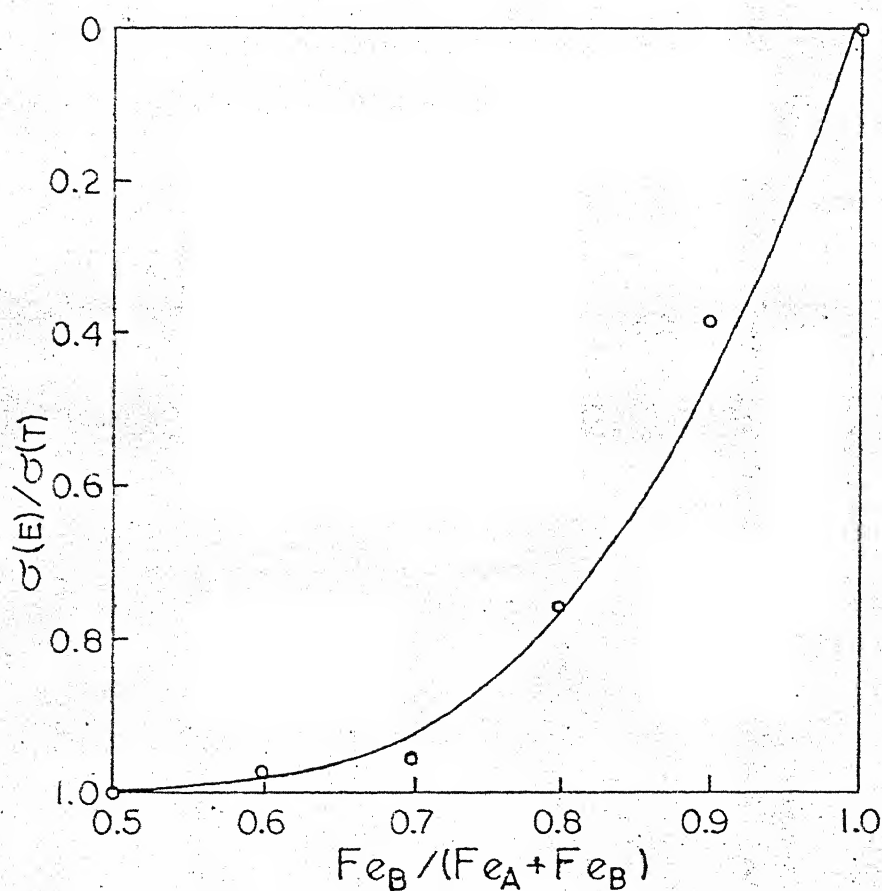


Fig. 11 Plot of the ratio of the experimental magnetic moment to the theoretical value $\sigma(E)/\sigma(T)$ for Ni-Zn-ferrite versus $Fe_B/(Fe_A + Fe_B)$, the numbers of Fe in B sites to the total Fe

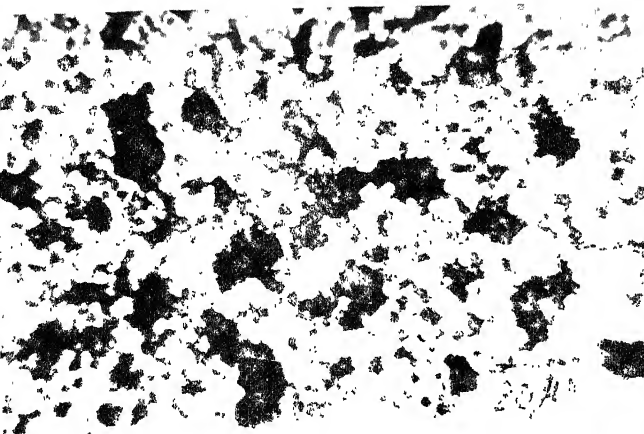


Fig. 9(iv)

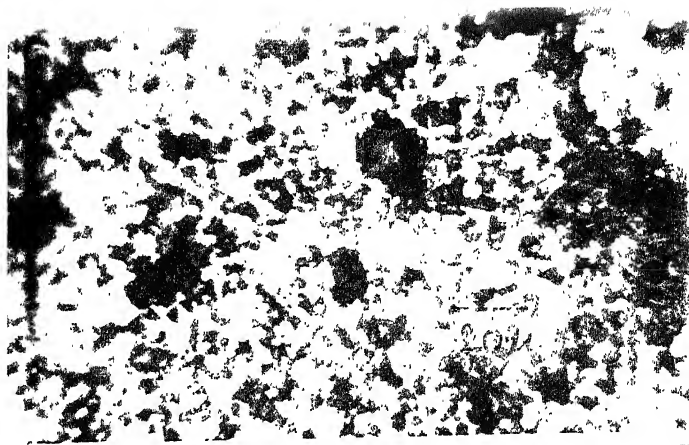


Fig. 9(v)

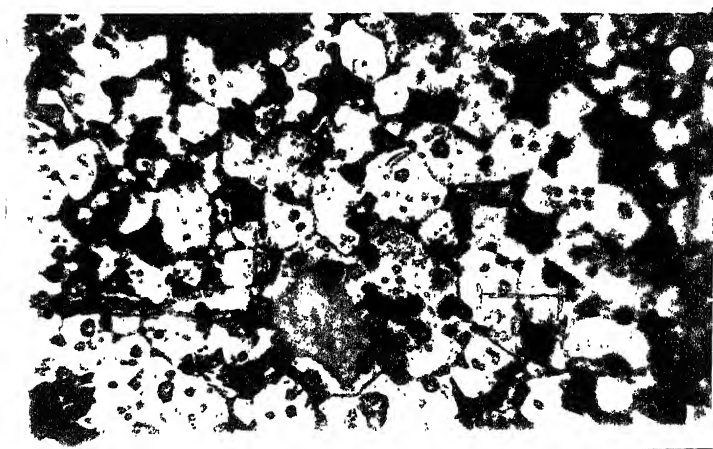


Fig. 9(vi)

Fig. 9. Photomicrographs of sintered ferrites with varying percentage of Ti^{+4} (etched with boiling HCl)

9(iv) Sintered at 1250°C for 20 hrs, 2% TiO_2

9(v) Sintered at 1250°C for 20 hrs, 5% TiO_2

9(vi) Sintered at 1250°C for 20 hrs, 10% TiO_2

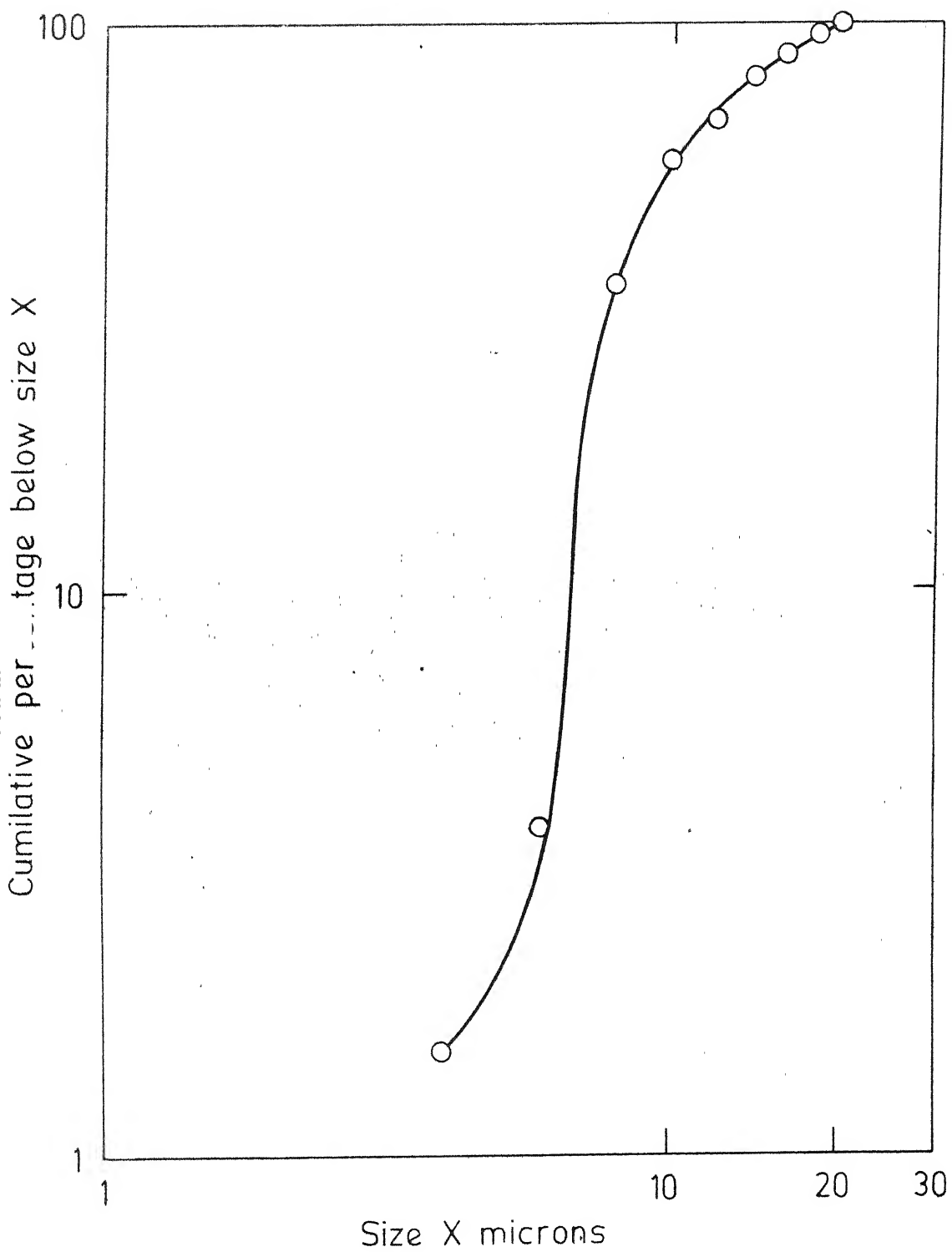


fig.10 - Particle size distribution of ground ferritised material.

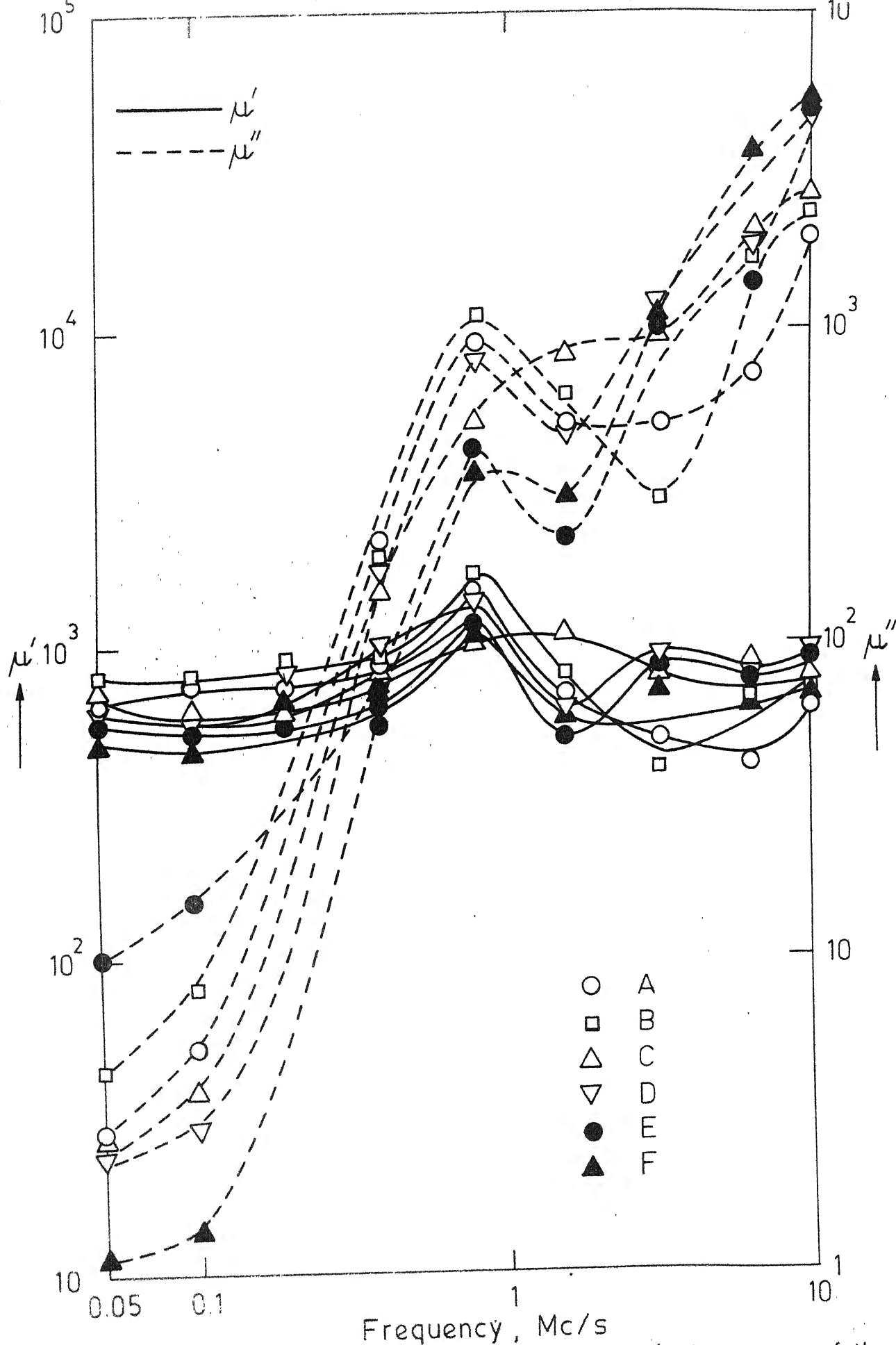
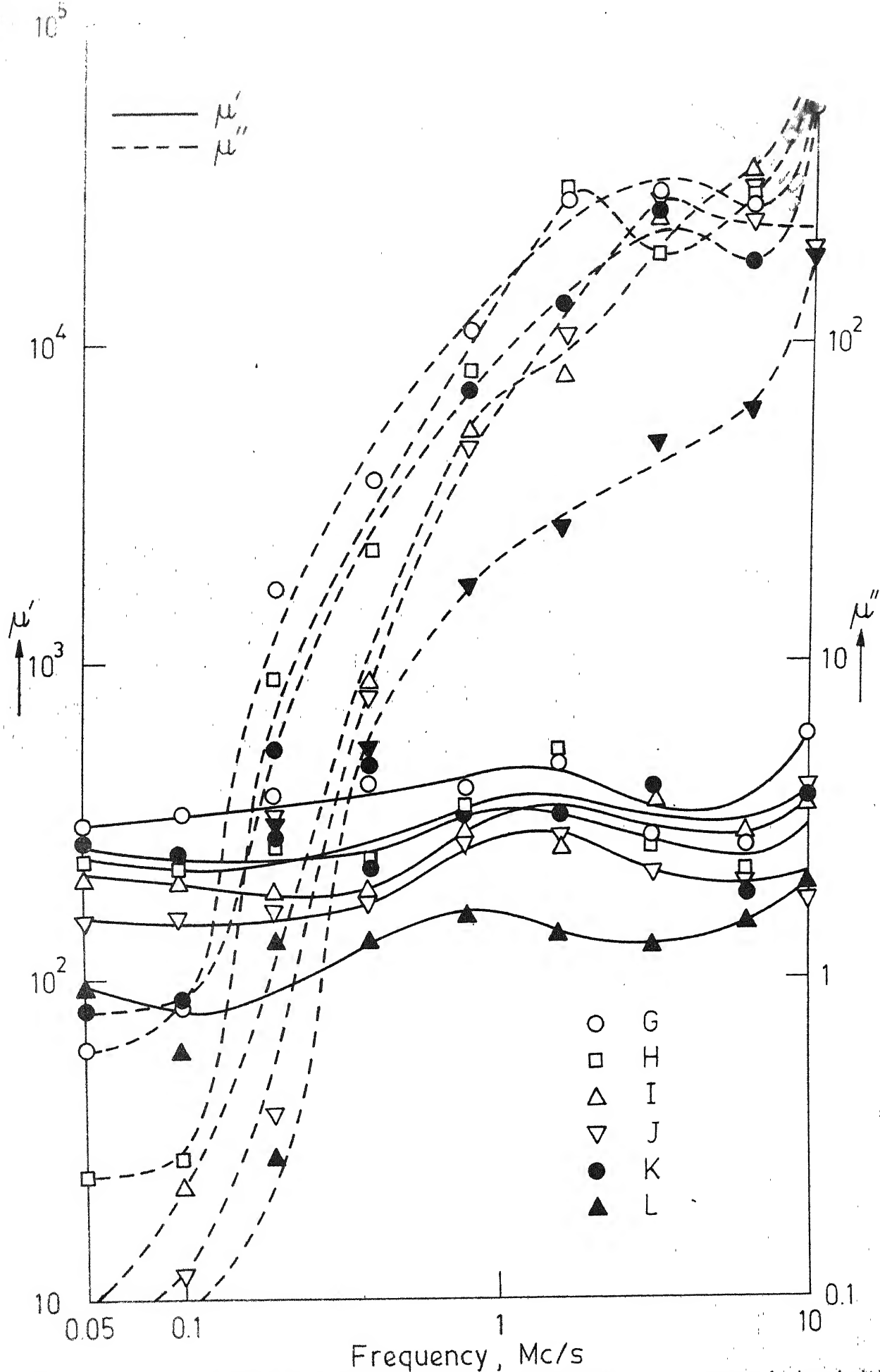


Fig.11-Frequency dependence of the real and imaginary parts of the initial permeability μ' and μ'' respectively of different compositions of Ni-Zn ferrite sintered at 1250°C for 20 hours.



12-Frequency dependence of the real and imaginary parts of the initial permeability μ' and μ'' respectively of different compositions of Ni-Zn ferrite sintered at 1250°C for 5 hours.

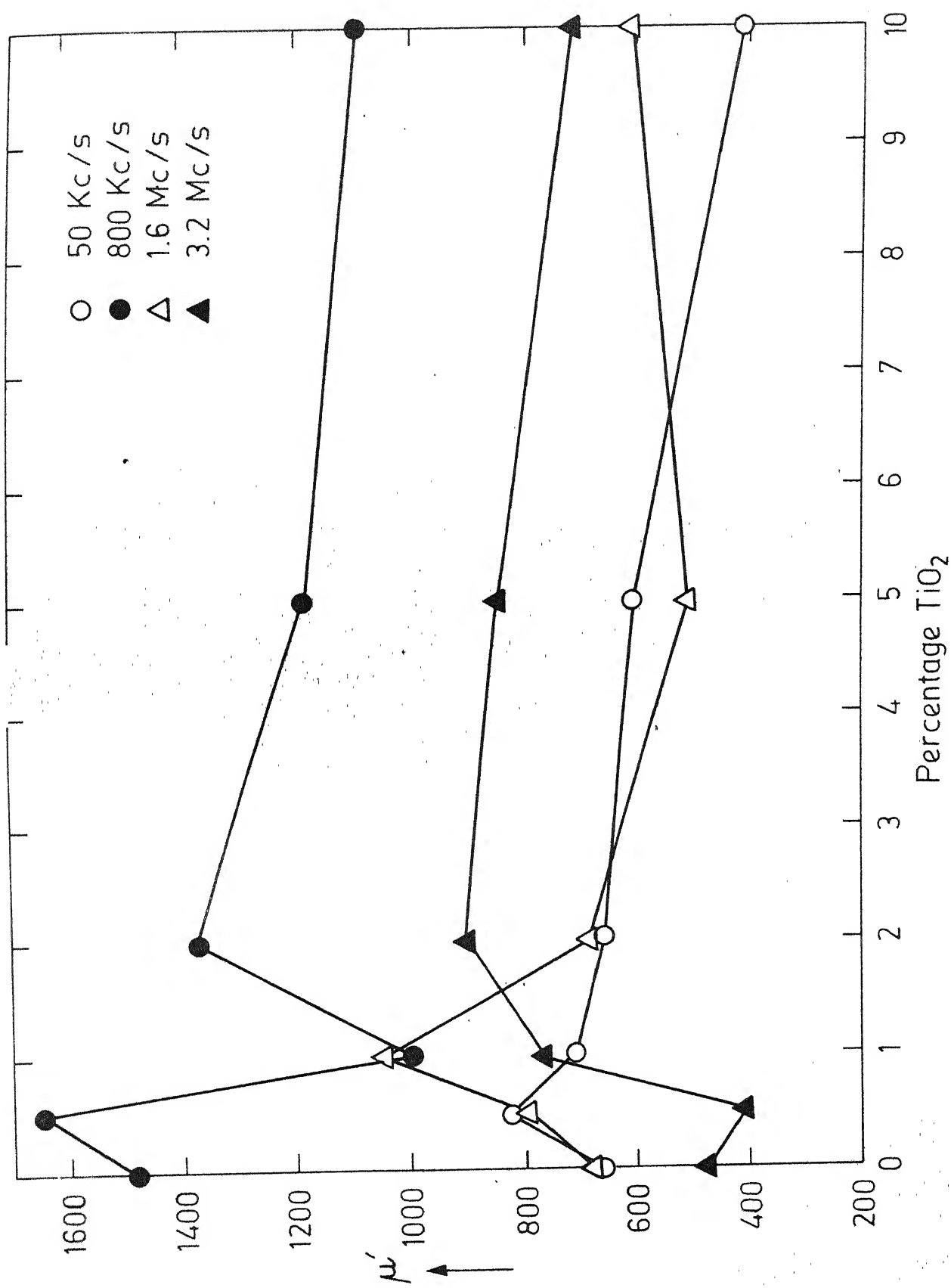


Fig. 13 - Variation of real part of initial permeability μ' with addition of TiO₂ in Ni-Zn ferrite sintered at 1250°C for 20 hours.

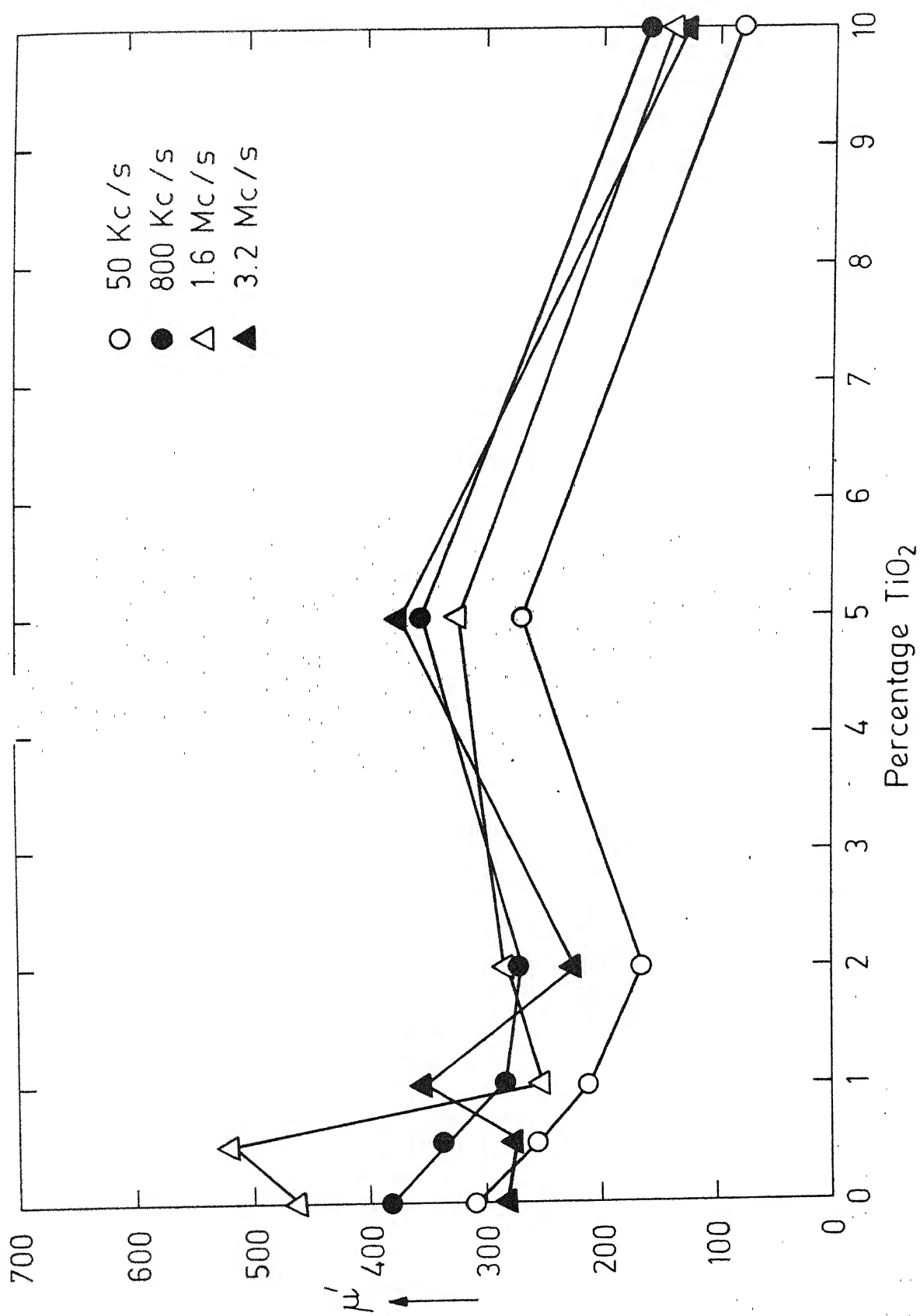


Fig. 14 - Variation of real part of permeability μ' with addition of TiO_2 in Ni-Zn ferrite sintered at 1250°C for 5 hours.

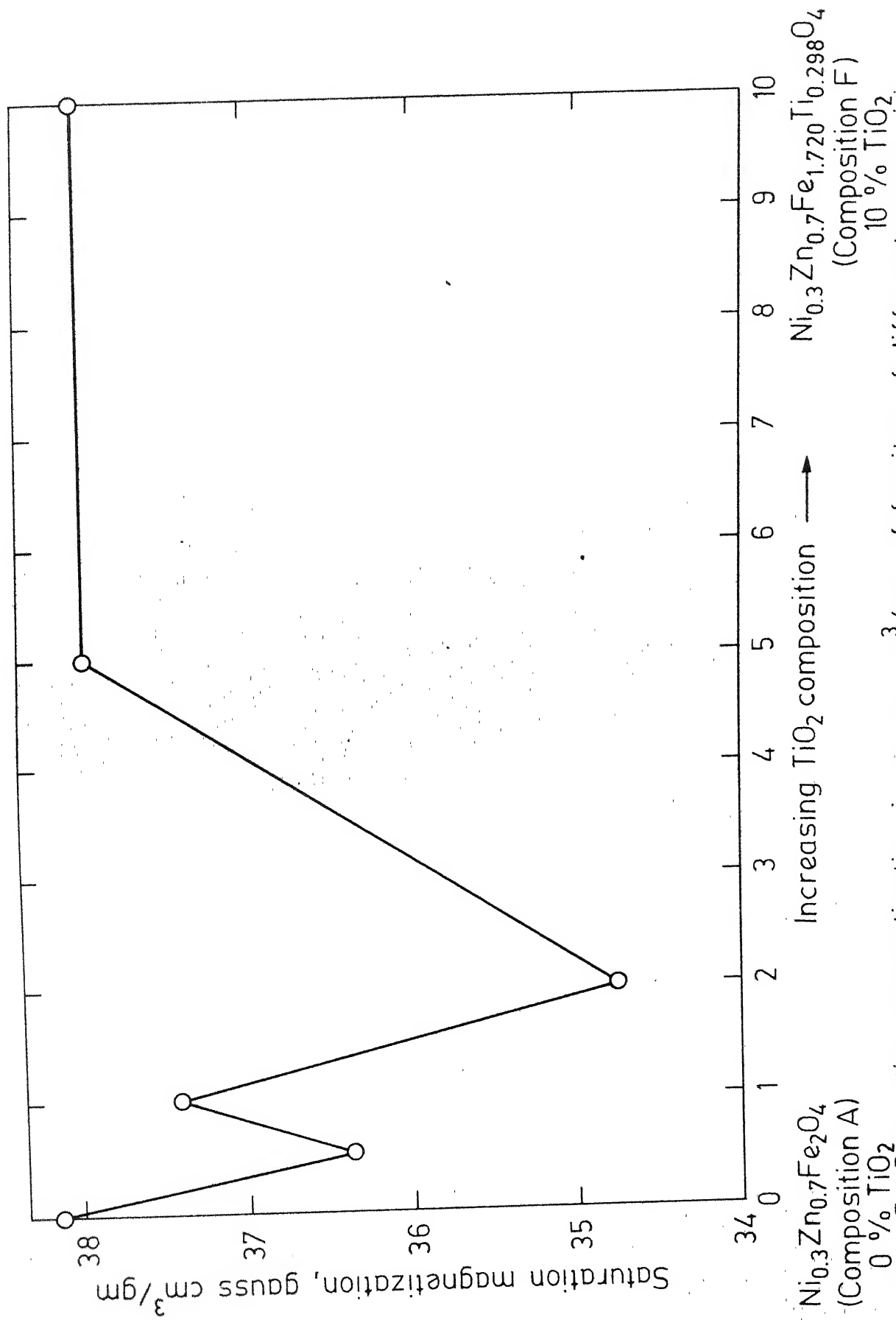


Fig. 15 - Saturation magnetization in gauss cm³/gm of ferrites of different compositions.

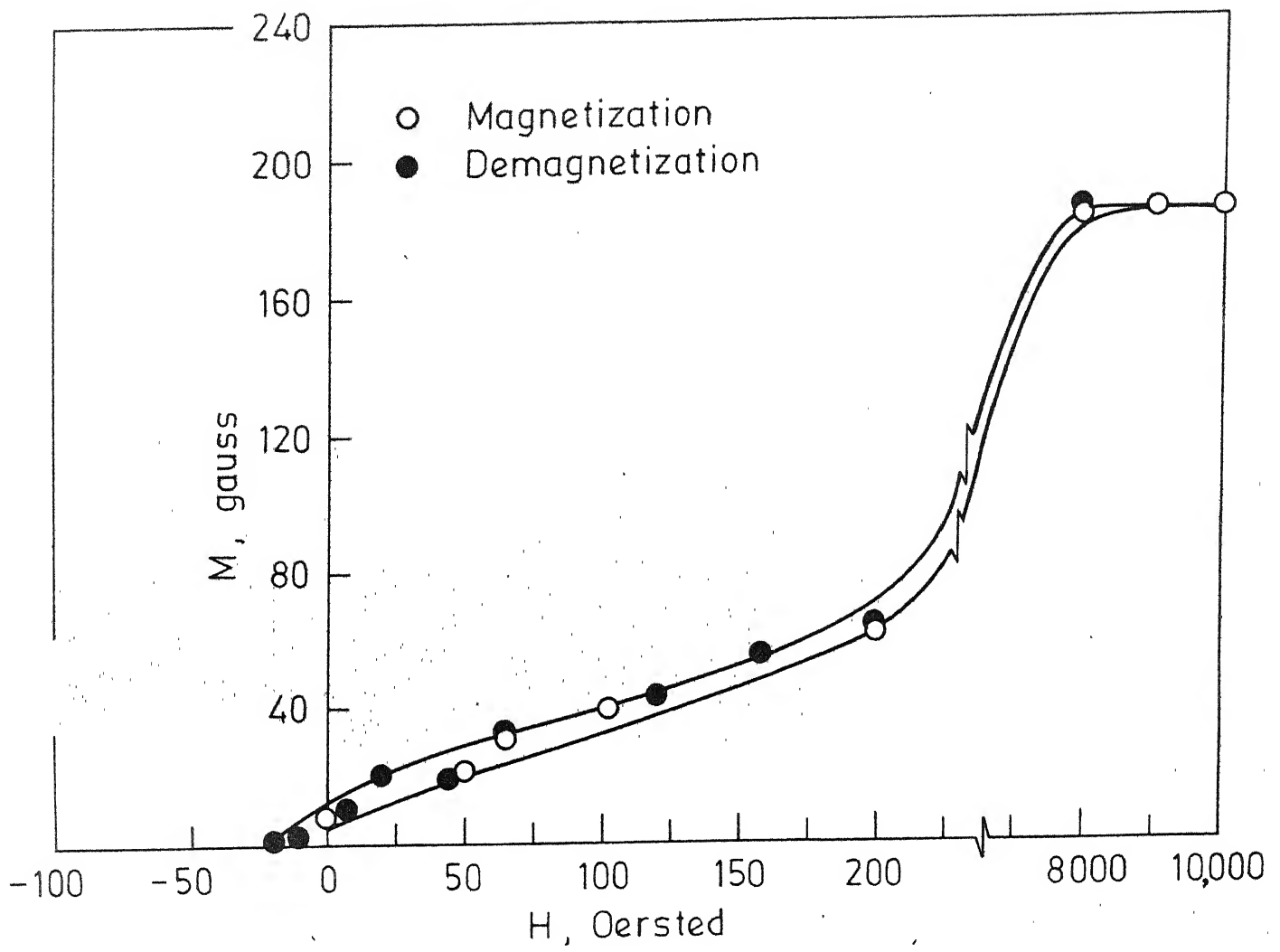


Fig. 16 - M - H curve of $\text{Ni}_{0.3}\text{Zn}_{0.7}\text{Fe}_2\text{O}_4$ sintered at 1250°C for 20 hours.

REFERENCES

1. D.J. Craik - "Structure and properties of magnetic materials - Pion Ltd., London (1971), p. 57.
2. J. Smit and H.P.J. Wijn - "Ferrites" - Philips Technical Library, Eindhoven (1959), p. 270.
3. A. Broesevan Groenour, P.F. Bongers and A.L. Stuyts - "Magnetism, microstructure and crystal chemistry of spinel ferrites" - Mat. Sci. Eng., 3, (1968), p. 317.
4. ibid - p. 314.
5. ibid - p. 315.
6. W.D. Kingery - "Introduction to Ceramics" - John Wiley and Sons, New York (1963), p. 753.
- 6A. A. Broesevan Groenour, P.F. Bongers and A.L. Stuyts - "Magnetism, microstructure and crystal chemistry of spinel ferrites" - Mat. Sci. Eng., 3, (1968), p. 320.
7. S. Chikazumi and S.H. Charap - "Physics of Magnetism" - John Wiley and Sons, New York (1964), p. 327.
8. ibid - p. 328.
9. A.I. Pil'shchikov and V.I. Dudkin - "Ferromagnetic resonance in the presence of domain structure" - Soviet Phys. Solid State, Vol. 8, No. 12, (1967), p. 2895.
10. R.A. Waldron - "Ferrites - An introduction for microwave engineers" - D. Van Nostrand Company (1961), p. 53.
11. J.C. Slonczewski - "Origin of magnetic anisotropy in cobalt substituted magnetic" - Phys. Rev. (B), Vol. 110, No. 6, (1958), p. 1341.
12. L.R. Bichford, J. Pappis and L.L. Stull - "Magnetostriiction and permeability of magnetic and co-substituted magnetite" - Phys. Rev. 99, (1955), p. 1210.
13. F. Voigt - "The effect of magnetic field annealing on the temperature dependence of the initial permeability of cobalt containing Ni-Zn ferrite" - Phys. Stat. Solidi, 2, (1962), p-k-27.

14. J. Kulikowski - "The effect of the oxidation degree on the temperature dependence of the initial permeability of Ni-Zn ferrites with excess Fe_2O_3 and small co-addition" - Przegl Elektron, (1965). *Chem. Abs.* (1968) 17183P
15. I. Mikanu - "Roll of induced anisotropy in magnetic spectra of co-substituted Ni-Zn ferrite" - Jap. J. Appl. Phys., 12 (5), (1973), p. 678.
16. P. Hansen and R. Krishnan - "Anisotropy and magnetostriction of 4d and 5d transition metal ions in garnets and spinel ferrites" - J. De Physique, (1977), p. c1-147.
17. R. Krishnan and V. Cagan - "Anisotropy and magnetostriction of Cr^{+3} ions in NiFe_2O_4 " - J. of Appl. Phys., 42, (1971), p. 1639.
18. L.R. Maxwell and S.J. Pickart - "Magnetic and crystalline behaviour of certain oxide systems with spinel and perovskite structure" - Phys. Rev. 96, (1954), p. 1501.
19. C. Guillard, B. Zega and G. Villers - "The effect of alkali and alkaline earth ions on the initial permeability of Mn-Zn ferrite" - Compt. Rend, 242, (1956), p. 2312.
20. M.S. Bekibulatov and Y.M. Khachetryan - "Static magnetic properties of Ni-Cu-Zn ferrites" - Fiz-Fiz-Khin-Svoistva. Ferritov. Mater. Dokl. Vses. Sovetskoy, 4th Minsk, (1966), p. 137.
21. R. Krishnan - "Magnetic anisotropy and resonance line width in rare earth doped nickel-iron-oxide crystal" - J. Phys. Colloq., (1971), p. c1-148.
22. J. Tasaki and T. Izushi - "Behaviours of additives in ferrites" - Journal De Physique, (1977), p. c-175.
23. E.W. Gorter - "Saturation magnetization and crystal chemistry of ferrimagnetic oxides" - Philips Res. Rep., 9, (1954), p. 321.
24. A. Broesevan Groenour, P.F. Bongers and A.L. Stuyts - "Magnetism, microstructure and crystal chemistry of spinel ferrites" - Mat. Sci. Eng., 3, (1968), p. 320.
25. *ibid* - p. 322.

26. Stijntjes et.al. - "Permeability and conductivity of titanium substituted Mn-Zn ferrite" - Philips Res. Rep., 25 (2), (1970), p. 95.
27. A. Broesevan Groenour, P.F. Bongers and A.L. Stuyts - "Magnetism, microstructure and crystal chemistry of spinel ferrites" - Mat. Sci. Eng., 3, (1968), p. 325.
28. S.K. Banerjee and W.O. Reilly - "Coercivity of Fe^{+2} in octahedral sites of Fe-Ti spinels" - I.E.E.E. Trans. Magnetism, (1966), p. 463.
29. Hoehne et.al. - "Induced magnetic anisotropy in titanium doped ferrites" - Phys. Stat. Solidi - A, 22 (1), (1974), p. K99.
30. A. Broesevan Groenour, P.F. Bongers and A.L. Stuyts - "Magnetism, microstructure and crystal chemistry of spinel ferrites" - Mat. Sci. Eng., 3, (1968), p. 325.
31. ibid - p. 326.
32. D.J. Craik - "Structure and properties of magnetic materials" - Pion Ltd., London, (1971), p. 204.
33. A. Broesevan Groenour, P.F. Bongers and A.L. Stuyts - "Magnetism, microstructure and crystal chemistry of spinel ferrites" - Mat. Sci. Eng., 3, (1968), p. 327.
34. J.E. Burke - "Grain growth in ceramics" - Kinetics of high-temperature processes - Editor W.D. Kingery, John Wiley and Sons, New York, (1959), p. 109.
35. W.B. Boast - "Principles of electric and magnetic fields" - Harper and Brothers, New York, (1956), p. 248.
36. S.K. Gupta - "Effect of processing conditions and microstructure on the magnetic spectrum of Ni-Zn ferrite" - M.Tech. Thesis, I.I.T. Kanpur, (1976), p. 15a.
37. D.L. Johnson and L. Berrin - "Grain boundary diffusion in the sintering of oxides" - Proc. Int. Conf. on "Sintering and related phenomena" - June (1965).
38. R.W. Grinshaw - "The chemistry and physics of clays and allied ceramic materials" - Ernest Benn Ltd., (1971), p. 82.
39. J. Smith and H.P.J. Wijn - "Ferrites" - John Wiley and Sons, (1959), p. 157.
40. M.B. Stout - "Basic electrical measurements" - Prentice-Hall Inc., (1961), p. 304.

APPENDIX I

DERIVATION OF FORMULAE USED IN Q-METER MEASUREMENTS⁴⁰

Q-meter is an exceedingly useful instrument for measuring the characteristics of coils and capacitors at radio frequencies. Derivation of the formulae used in Q-meter measurements are given below.

Series Connection

If the circuit is resonated at a value C_1 , with a Q-reading of Q_1 before introducing the unknown, then

$$\frac{1}{\omega C_1} = \omega L \quad (I-1)$$

where L = Inductance

$\omega = 2\pi f$, where f = frequency

C_1 = Capacitance

and

$$Q_1 = \frac{\omega L}{R} = \frac{1}{\omega C_1 R} \quad (I-2)$$

where R = Resistance.

If an unknown with series components X_s (Inductive or Capacitive reactance) and R_s is introduced in series, the new readings are C_2 and Q_2 , then

$$X_s = \frac{1}{\omega C_2} - \omega L = \frac{1}{\omega C_2} - \frac{1}{\omega C_1}$$

or

$$X_s = \frac{C_1 - C_2}{\omega C_1 C_2} \quad (I-3)$$

(Inductive if $C_1 > C_2$

Capacitive if $C_1 < C_2$)

$$R_s = \frac{X_2}{Q_2} - \frac{X_1}{Q_1} = \frac{1}{\omega C_2 Q_2} - \frac{1}{\omega C_1 Q_1} = \frac{C_1 Q_1 - C_2 Q_2}{\omega C_1 C_2 Q_1 Q_2}$$

where X_1 = Reactance without the material

X_2 = Reactance of material and system.

$$\text{Therefore } Q_x = \frac{X_s}{R_s} = \frac{(C_1 - C_2) Q_1 Q_2}{C_1 Q_1 - C_2 Q_2} \quad (I-4)$$

where $Q_x = Q$ of the unknown.

Parallel Connection

The characteristics of an unknown connected in parallel are expressed most simply in terms of parallel X_p and R_p . After the preliminary balance, as before, the addition of X_p requires an increase in tuning capacitance (if X is inductive) to a new value C_2 , which may be regarded practically as C_1 resonating L as in the preliminary balance, and $(C_2 - C_1)$ resonating the unknown X_p ,

$$\text{or } X_p = \frac{1}{\omega(C_2 - C_1)} \quad (I-5)$$

$$\text{Again } \frac{1}{R_p} = \frac{\omega C_1}{Q_2} - \frac{R}{R^2 + \omega^2 L^2}$$

$$\begin{aligned}
&= \frac{wC_1}{Q_2} - \frac{1}{R} \cdot \frac{1}{1 + \frac{w^2 L^2}{R^2}} \\
&= \frac{wC_1}{Q_2} - \frac{1}{RQ_1^2}
\end{aligned}$$

(Replacing $1 + Q_1^2$ by Q_1^2 , since $Q_1 \gg 1$).

$$\text{Using } Q_1 = \frac{1}{wC_1 R}, \text{ we get, } R_p = \frac{Q_1 Q_2}{wC_1 (Q_1 - Q_2)} \quad (\text{I-6})$$

$$\text{Therefore } Q_x = \frac{R_p}{X_p} = \frac{(C_2 - C_1) Q_1 Q_2}{C_1 (Q_1 - Q_2)} \cdot \quad (\text{I-7})$$

APPENDIX II

ERRORS AND THEIR ELIMINATION IN Q-METER MEASUREMENTS

The apparently simple Q-meter measurement requires some discussions. There are many types of errors which should be considered to avoid peculiar results. We did following types of experiments and got different conclusions from them.

- (1) Say we have wound the toroid with N turns and we have got C_2 , Q_2 (see Appendix I for meaning of C_2 , Q_2). We can get effectively same N number of turns by taking two different wires and giving N number of turns by each wire in two different directions (that is one is clockwise and another anticlockwise) and connecting them at the two terminals. At this C_2 in the second case is increased by 0.9% approximately and Q_2 in the 2nd case increased by 3.7% approximately when the measurement was done at 1 megacycle/sec frequency, using 9 turns for small toroid. Increase in C_2 in the second case is due to cancellation of some stray capacitance due to winding in two parts. Decrease in Q_2 is due to use of more wire, so resistance loss etc. decreased Q value.
- (2) We used N number of turns by giving winding with double turns i.e. we used $N/2$ windings with double wire. In this case there was no change in C_2 and Q_2 value.
- (3) By taking two wires of same length and giving same number of turns in same direction (i.e. either clockwise or anticlockwise

winding) one should expect cancellation of L . But we got some C_2 value, which indicates that there are some stray capacitance. The value of stray capacitance depends on type of material, size and shape of the toroid, type of winding etc.

- (4) Use of too long wire is to be avoided as it has inductance and/or capacitance effect, otherwise it will introduce errors in measurements. As for example at 750 Kcycle use of 1" long wire (36 gauge insulated copper wire) decreased C_2 value to 2.2% approximately and Q value decreased to 5.3% approximately. In this case first the standard coil was directly connected with the Q-meter. In the second case standard coil was connected with Q-meter by 1" long wire.
- (5) We used another thick wire to compare the effects of thin wire and thick wire. For the case of thick wire C_2 and Q_2 value both decreased. The decrease in C_2 is due to extra capacitance or inductance effect due to thickness. Due to more thickness, the eddy current loss is greater, so Q value also decreased. The percentage decrease in C_2 and Q_2 is dependent on thickness of the wire, frequency of measurement, length of wire etc.
- (6) We cannot use direct measurement without using standard coil. Then we will get circuit Q , it is very difficult to distinguish it from material Q . Circuit Q will vary with number of turns and other factors, but material Q is constant at

constant frequency. So we have to use either series or parallel connection method.

- (7) The main point is to choose standard coil of proper inductance value and proper number of turns and proper size of the toroid so that inductance of standard coil does not differ from that of the toroid by many orders of magnitude. Otherwise inductance of one will control the final result. As for example at 50 Kcycles/sec frequency we measured the value of C_2 and Q_2 of small toroid using 10 number of turns. Inductance of standard coil used was of the order of millihenry, whereas assumed inductance of the toroid at 10 number of turns was of the order of microhenry. We measured C_2 and Q_2 of a toroid of same size, made of plastic under same conditions. Surprisingly we got same value of C_2 and Q_2 for plastic and ferrite, as if ferrite and plastic are of same permeability. The reason is that due to vast difference of inductance of the standard coil and toroid, Q-meter was unable to distinguish between plastic and ferrite.

So in our measurements we changed number of turns with change of frequency (consequently with change of inductance of the standard coil) and we also used small toroids and large toroids accordingly and to increase the C_2 range we used bank of capacitors.

(8) We plotted L vs. N^2 curve (L = Inductance). According to equation (2.3), it should be straight line and it will pass through origin. At lower frequencies we got straight line, at higher frequencies the matching was not good, there we used straight line approximation. But both in lower frequencies and higher frequencies the straight line did not pass through origin indicating presence of stray capacitance or inductance. So we used slope method to calculate μ' and hence we used the formula (2.4) that is

$$(L_1 - L_2) = \text{Constant} \times \mu' \times (N_1^2 - N_2^2) \text{ to calculate } \mu'.$$

(N_1 and N_2 are number of turns).

Date **SLIP** **A 55424**

This book is to be returned on the
date last stamped. _____

[illegible]

CD 6.72.9

ME-1978-M-SEN-EFF